GREEN SYNTHESIS OF CuO-CaO BINARY NANOPARTICLES AND ITS APPLICATION FOR PHOTOCATALYTIC DEGRADATION OF PETROLEUM WASTEWATER

BY

Aiyevbekpen Clinton EHIGIE
PG/LSC2110441

DEPARTMENT OF SCIENCE LABORATORY TECHNOLOGY
FACULTY OF LIFE SCIENCES
UNIVERSITY OF BENIN,
BENIN CITY.

NOVEMBER, 2025

GREEN SYNTHESIS OF CuO-CaO BINARY NANOPARTICLES AND ITS APPLICATION FOR PHOTOCATALYTIC DEGRADATION OF PETROLEUM WASTEWATER

BY

Aiyevbekpen Clinton EHIGIE
PG/LSC2110441

THESIS SUBMITTED TO THE COLLEGE OF POSTGRADUATE STUDIES IN PARTIAL FULFILMENT FOR THE AWARD OF MASTER OF SCIENCE (CHEMISTRY TECHNIQUES), IN THE DEPARTMENT OF SCIENCE LABORATORY TECHNOLOGY, FACULTY OF LIFE SCIENCES, UNIVERSITY OF BENIN, BENIN CITY

NOVEMBER, 2025

CERTIFICATION

This is to certify that this research was carried out by Aiyevbekpen Clinton EHIGIE with Mat No: PG/LSC2110441 of the Department of Applied Chemical Science Laboratory Technology, Faculty of Science Laboratory Technology, University of Benin, Edo State.

_____ _____

PROF. J. O. OSARUMWENSE DATE
SUPERVISOR

_____ _____

PROF. J. O. OSARUMWENSE DATE
H.O.D

_____ _____

EXTERNAL EXAMINER DATE

DEDICATION

This work is dedicated to God Almighty, the source and sustainer of my life, and to my late father Mr. William Osiomwanuri Ehigie whose desire was to see me earn a Ph.D. degree, Daddy, I miss you greatly.

ACKNOWLEDGEMENTS

My sincere gratitude goes to God Almighty who has given me life and grace for this program. I also wish to heartily appreciate my Supervisor, Prof. J. O. Osarumwense for his fatherly advice, corrections, and suggestions that make this work a reality. I will not fail to appreciate the Postgraduate coordinator, Prof. E. O. Oshomoh, and the entire PG board members of the Faculty of Science Laboratory Technology for their contributions towards the success of this program. I also wish to sincerely appreciate my darling wife, Minister Flourish Aiyevbekpen-Ehigie, for her unending support throughout this program, my beloved children, Efeomo, Efeosasere, and Etinosasere for their prayers. My appreciation also goes to beloved mother, Mrs. Mabel Ehigie, and my late father, Mr. William Osiomwanuri Ehigie, as well as my siblings, whose encouragement I recieved me, especially in trying moments during this program. I will forever be grateful to them. I wish to thank my friends and colleagues in the office, Mr. Lucky Eduwuyofo, Mr. Osagie Amayo, Mr.Idahosa Morgan, Mr.Oligie Mc.Henry Dr. Mrs Emerebe, Mrs. Otoe and others, thank you so much for your contribution to my success.

TABLE OF CONTENTS

LIST OF FIGURES

LIST OF TABLES

LISY OF PLATES

ABSTRACT

The green synthesis of metal oxide nanoparticles has garnered substantial interest in recent years due to their promising applications in environmental remediation. This study presents the synthesis of copper oxide nanoparticles and calcium oxide-copper oxide binary nanoparticles utilizing onion (Allium cepa) peel extract for photocatalytic degradation of petroleum wastewater. CuO, and CaO – CuO nanoparticles were synthesized in this study following already established methods as reported in journals.

Characterization of the synthesized nanoparticles was performed employing various analytical techniques, including X-ray diffraction (XRD), scanning electron microscopy (SEM), dynamic light scattering (DLS), and Fourier Transform Infrared spectroscopy (FTIR). The photocatalytic performance of the synthesized nanoparticles was systematically assessed for the degradation of petroleum wastewater under sunlight irradiation.

Results indicated that the calcium oxide-copper oxide binary nanoparticles demonstrated significantly enhanced photocatalytic activity compared to the copper oxide nanoparticles, achieving a degradation efficiency of 95.76 %. This superior photocatalytic performance of the binary nanoparticles can be attributed to the synergistic effect of the p-n heterojunction between calcium oxide and copper oxide, which enhances spatial separation of photogenerated electron – hole pairs, thus improving the photodegradation of the wastewater. The green synthesis methodology employed in this study represents a cost-effective and environmentally sustainable approach for the production of metal oxide nanoparticles intended for environmental applications.

CHAPTER ONE

INTRODUCTION

1.1: BACKGROUND OF STUDY

The increasing global dependence on petroleum hydrocarbons for energy production and industrial activities has led to a significant environmental problem: the persistent contamination of ecosystems with petroleum byproducts (Ossai *et al*., 2020). Incidents of accidental spills, improper waste disposal, and industrial discharges introduce a complex array of persistent organic pollutants (POPs) into both aquatic and terrestrial environments. Among these pollutants are resistant compounds such as polycyclic aromatic hydrocarbons (PAHs) and total petroleum hydrocarbons (TPH), which contribute to the degradation of ecological health (Ossai *et al*., 2020). These pollutants exhibit carcinogenic, mutagenic, and toxic characteristics, presenting significant hazards to human health, aquatic ecosystems, and agricultural productivity (Abdel-Shafy and Mansour, 2016). Conventional remediation methods, such as physical skimming, chemical dispersion, and biodegradation, face challenges including incomplete degradation, high costs, long treatment times, and the risk of creating toxic by-products (Sharma *et al*., 2024). The inadequacy of current methods has prompted an urgent search for innovative, efficient, and sustainable decontamination technologies.

In this regard, advanced oxidation processes (AOPs) have emerged as a promising solution, particularly heterogeneous photocatalysis, which has demonstrated notable effectiveness in mineralizing organic pollutants into harmless byproducts, such as carbon dioxide (CO_2) and water (H_2O) (Gaya and Abdullah 2008). These processes utilize semiconductor nanomaterials as

photocatalysts that, when exposed to light of appropriate energy, yield electron-hole (e^-/h^+) pairs. These charge carriers subsequently facilitate redox reactions, resulting in the formation of highly reactive oxygen species (ROS), including hydroxyl radicals (•OH) and superoxide anions ($•O_2^-$). Such reactive species indiscriminately engage with and decompose organic molecules (Fujishima *et al*., 2008). Titanium dioxide (TiO_2) has long served as the standard photocatalyst; however, its substantial band gap of approximately 3.2 eV limits its photocatalytic activity primarily to the ultraviolet (UV) spectrum. This spectral region encompasses merely a small fraction, around 4%, of the total solar radiation (Schneider *et al*., 2014). The constraints associated with traditional materials have catalysed a search for alternative semiconductors that are active under visible light. Among the noteworthy contenders, copper oxide (CuO) and calcium oxide (CaO) nanoparticles present promising characteristics. CuO, characterised as a p-type semiconductor with a narrow band gap ranging from 1.2 to 1.7 eV, demonstrates substantial absorption throughout the visible and near-infrared regions of the spectrum, which positions it as an effective solar light harvester (Zhang *et al*., 2014). Furthermore, CuO NPs are known for their catalytic activity and ability to generate ROS effectively (Ansari *et al*., 2016). Conversely, calcium oxide (CaO), although frequently categorized as a wide-band-gap material, exhibits significant surface basicity and a pronounced affinity for organic molecules. These properties can facilitate the adsorption of pollutants onto the catalyst surface, which is a crucial initial stage in the process of photocatalysis (Oghenefejiro *et al*., 2025). The strategic integration of these two distinct metal oxides into a binary nanocomposite represents an advanced methodology for the development of a more efficient photocatalytic system. The establishment of a heterojunction interface between calcium oxide (CaO) and copper oxide (CuO) serves to enhance the spatial separation of photogenerated electron-hole pairs. This configuration significantly reduces their recombination rate, resulting in a marked

improvement in quantum yield (Low *et al*., 2017). This synergy promises a composite material with superior performance compared to its individual components

However, the ecological benefits of a remediation technology can be annulled if the synthesis of the catalyst itself is polluting. Conventional physico-chemical methods for nanoparticle synthesis (e.g., sol-gel, co-precipitation, laser ablation) often involve high energy consumption, high temperatures and pressures, and the use of hazardous chemicals as reducing and capping agents, raising concerns about toxicity and environmental sustainability (Iravani, 2011). This paradox underscores the critical importance of green synthesis. This bio-inspired approach utilizes biological matrices—such as plant extracts, fungi, bacteria, or biopolymers—as eco-friendly replacements for chemical agents (Mittal *et al*., 2013). The phytochemicals present in plant extracts (e.g., flavonoids, alkaloids, terpenoids, and polyphenols) serve as effective reducing and stabilizing agents, governing the nucleation and growth of nanoparticles (Oghenefejiro *et al*., 2025).

Green synthesis approaches are typically conducted under ambient conditions, offering cost-effectiveness and producing nanoparticles with enhanced biocompatibility, stability, and distinctive morphologies. These characteristics often improve the catalytic activity of the nanoparticles (Kharissova *et al*., 2013; Haider *et al*., 2024). Therefore, this research is dedicated to integrating these cutting-edge concepts by exploring the green synthesis of calcium oxide and copper oxide nanoparticles and their binary composite for photocatalytic degradation of petroleum waste.

1.2: STATEMENT OF THE PROBLEM

The extensive pollution of ecosystems by petroleum waste, resulting from extraction, transportation, and industrial processes, poses a significant global environmental challenge (Ossai *et al*., 2020). This waste, comprising persistent and toxic organic pollutants such as polycyclic aromatic hydrocarbons (PAHs) and total petroleum hydrocarbons (TPH), poses severe risks to human health, aquatic life, and soil fertility due to its carcinogenic and mutagenic properties (Abdel-Shafy and Mansour, 2016). Conventional remediation approaches, including physical skimming, chemical dispersant application, and traditional bioremediation techniques, often demonstrate insufficient efficacy. These methods are often hindered by factors such as inefficiency, increased costs, prolonged treatment timelines, and the potential generation of secondary pollutants. Consequently, there exists a notable inadequacy in efficient technologies for environmental remediation (Adofo *et al*., 2022). This deficiency highlights the urgent need for the development of innovative, efficient, and sustainable remediation technologies.

Semiconductor-based heterogeneous photocatalysis has emerged as a powerful Advanced Oxidation Process (AOP) capable of mineralizing recalcitrant organic pollutants into harmless substances like CO_2 and H_2O (Gaya and Abdullah, 2008). However, the practical implementation of this technology faces three fundamental challenges:

1. **Limited Utilization of Solar Energy:** Titanium dioxide (TiO_2) is the most extensively studied photocatalyst, primarily demonstrating its activity under ultraviolet (UV) light, which constitutes only a small fraction of the solar spectrum, approximately 4%. This constraint limits the effectiveness of solar-driven photocatalytic applications and enhances the operational energy

demands, thereby compromising both the sustainability and economic feasibility of this technology (Fujishima *et al*., 2008; Gunawan *et al*., 2024)

2. **Rapid Recombination of Charge Carriers:** A significant limiting factor in the photocatalytic process is the swift recombination of photogenerated electron-hole (e^-/h^+) pairs, which occurs in numerous promising semiconductors active under visible light before they can engage in surface redox reactions (Schneider *et al*., 2014; Rostami *et al*., 2025). This recombination substantially diminishes both the quantum efficiency and the overall effectiveness of the degradation process.

3. **Unsustainable Synthesis of Nanomaterials:** Traditional chemical and physical approaches for the synthesis of photocatalytic nanoparticles frequently utilize toxic reagents, require substantial energy input, and produce hazardous by-products (Dhaka *et al*., 2023). This paradoxically positions the production of an agent intended for environmental remediation as a contributor to pollution, thereby undermining the fundamental tenets of green technology.

1.3: JUSTIFICATION OF STUDY

Investigations into alternative photocatalysts have highlighted materials such as copper oxide (CuO), recognized for its effectiveness in visible-light absorption (Singh *et al*., 2019), and calcium oxide (CaO), noted for its adsorptive and catalytic properties (Hemmami *et al*., 2024). However, significant research gaps remain in the existing literature. This study aims to address the critical void identified within this scholarly discourse.

1. **Underexplored Green Synthesis of CaO NPs.** While the green synthesis of some metal nanoparticles is well-documented, the bio-inspired synthesis route for calcium oxide (CaO) nanoparticles has limited exploration (Hemmami *et al*., 2024).

2. **Lack of Research on a Binary CaO-CuO Composite**: There is a significant lack of research focused on the synergistic integration of green-synthesized CaO and CuO into a binary nanocomposite. The possibility of establishing a p-n heterojunction at their interface, which could promote the spatial separation of charge carriers and improve photocatalytic efficiency, represents a novel and promising avenue that remains under investigated (Chen *et al*., 2024).

3. **Limited Application CaO-CuO composite to Complex Petroleum Waste:** Most photocatalytic research has primarily targeted the degradation of individual pollutants, like synthetic dyes (Mittal *et al*., 2013). However, there has been limited systematic investigation into using a green-synthesized CaO-CuO binary composite for breaking down complex, real-world mixtures such as petroleum waste, which includes a variety of persistent hydrocarbons.

The central issue addressed by this research is the absence of a sustainable, visible-light-activated, and highly efficient photocatalytic system specifically tailored for the remediation of petroleum-derived waste. This challenge arises from the inherent limitations of current catalysts and their synthesis methodologies. This study aims to tackle this problem by innovatively bridging existing gaps through the green synthesis of calcium oxide (CaO) and copper oxide (CuO) nanoparticles, followed by the formulation of their binary composite to harness synergistic effects. Additionally, the research involves a comprehensive evaluation of the composite's performance against authentic petroleum waste, thereby proposing a holistic and environmentally friendly solution.

1.4: AIM OF STUDY

The aim of this study was to synthesize CaO-CuO nanocomposite using onion peel as reducing agent for the photodegradation of petroleum wastewater.

1.5: SPECIFIC OBJECTIVES

To achieve the above aim, the following specific objectives were set. They are to:

- extract phytochemicals from pulverized onion peel by decoction
- use the onion peel extract to synthesize copper oxide nanoparticles
- use the onion peel extract to synthesize the binary oxides calcium and copper nano particles.
- characterize the synthesized nanoparticles: XRD, FTIR, SEM-EDS, and DLS
- source for petroleum wastewater and carry out physicochemical characterization of the petroleum wastewater
- carry out the photocatalytic degradation of the petroleum wastewater.
- optimize the degradation process and use the optimized condition to determine the rate of degradation
- characterize the treated wastewater

1.6: SCOPE OF STUDY

The study focuses on the green synthesis of copper oxide (CuO) and calcium oxide-copper oxide (CaO-CuO) nanoparticles using onion peel extract, and their application in photocatalytic degradation of petroleum wastewater. It entails:

(1) Extracting the bioactive compounds from onion peel powder using decoction.

(2) Synthesizing copper oxide nanoparticles (CuONP_S) using the onion peel extract

(3) Synthesizing the calcium oxide-copper oxide nanocompsites (CaO-CuO NP_S) using the onion peel extract

(4) Analysing the synthesized NP_S using XRD, FTIR, SEM-EDS and DLS

(5) Sourcing petroleum wastewater and assessing its physicochemical properties

(6) Investigating the photocatalytic degradation of petroleum wastewater using CuO and CaO-CuO NP_S.

(7) Optimising degradation conditions and determining the degradation rate.

(8) Evaluating the quality of the treated petroleum wastewater.

CHAPTER TWO

LITERATURE REVIEW

2.1: NANOPARTICLES

Nanoparticles are tiny materials that have specific physicochemical properties different from bulk materials of the same composition. They usually measure between 1 to 100 nanometers, making them roughly 1,000 times thinner than human hair (Prathamesh *et al*., 2024). The size of these particles is an important aspect that influences their characteristics and behavior. When the size of particles reduces to the nanoscale, their physical, chemical, and optical properties can change significantly. In general, as the size of nanoparticles decreases, their surface area to volume ratio increases, leading to a greater number of surface atoms and higher reactivity (Altammar, 2023).

Nanoparticles have attracted significant interest due to their distinctive properties and diverse applications across various fields, including catalysis, environmental remediation, and biomedicine. Among these, Calcium Oxide (CaO) and Copper Oxide (CuO) nanoparticles have emerged as significant subjects of research owing to their unique attributes and extensive utility (Nasir *et al*., 2024; Naseem and Durrani, 2021). CaO nanoparticles are particularly recognized for their robust basicity, biocompatibility, and high reactivity, which render them valuable in catalysis, biodiesel production, and environmental remediation. Conversely, CuO nanoparticles, classified as p-type semiconductors, are esteemed for their catalytic, antimicrobial, and electrochemical properties, leading to applications in sensing, energy storage, and biomedicine (Hemmami *et al*., 2022; Oghenefejiro *et al*., 2025). Traditional methods of synthesis frequently utilize toxic chemicals and operate under extreme conditions. Alternatively, green synthesis approaches that

harness biological resources such as plant extracts, bacteria, and fungi provide environmentally friendly, cost-effective, and sustainable alternatives (Khan *et al*., 2020).

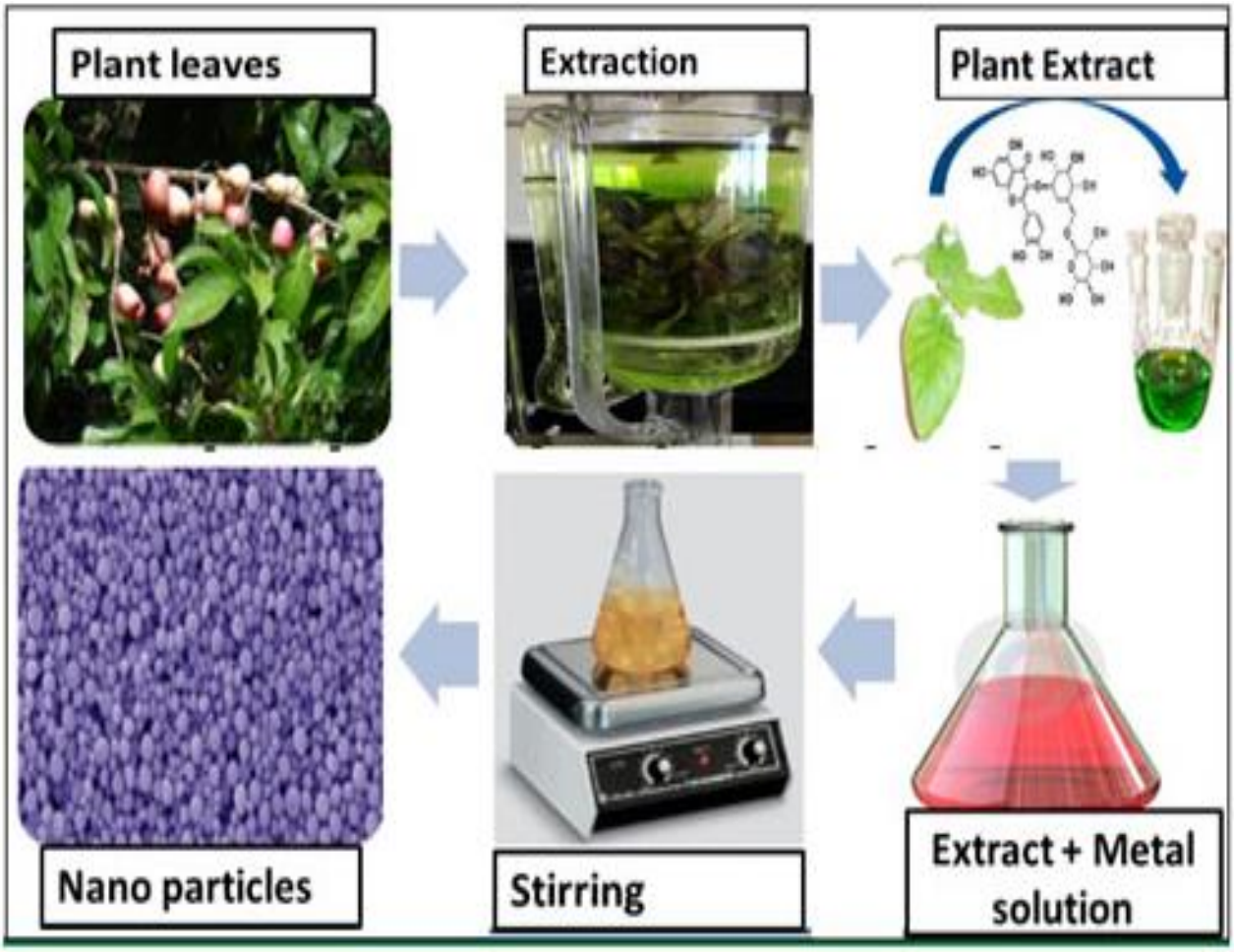

Plate 2.1: Green synthesis of metal oxide nanoparticles (Ahmed *et al*., 2018)

2.1.1: GREEN SYNTHESIS OF CALCIUM OXIDE NANOPARTICLES

Calcium oxide (CaO) nanoparticles are vital in environmental and industrial applications such as wastewater treatment and cement manufacturing. CaO NPs are known for their high surface reactivity, basicity, and non-toxic nature. While not a classic semiconductor like TiO_2, CaO can exhibit photocatalytic activity under UV light, primarily through the generation of superoxide radicals ($O_2^{\bullet -}$) due to its wide bandgap (>5 eV). Its primary role in composite systems is often to provide adsorption sites for pollutants and enhance the separation of photogenerated charge carriers (0ghenefejiro *et al*., 2025).

Recent studies have demonstrated the potential of plant extracts in synthesizing CaO nanoparticles. For example, Kumar *et al*. (2019) reported the successful synthesis of CaO nanoparticles using *Azadirachta indica* (neem) leaf extract, which acted as both a reducing and capping agent. The process was simple, environmentally benign, and yielded nanoparticles with desirable size and crystallinity. Oghenefejiro *et al*. (2025) conducted a study on the synthesis and antibacterial properties of calcium oxide nanoparticles (CaO NPs) derived from the extract of mango leaves (*Mangifera indica*), presenting a sustainable methodology for nanoparticle production. The synthesized CaO NPs were thoroughly characterized through dynamic light scattering (DLS), Fourier-transform infrared spectroscopy (FTIR), energy-dispersive X-ray spectroscopy (EDX), and scanning electron microscopy (SEM). The DLS analysis indicated an average particle size of 61.47 nm, while FTIR spectroscopy identified significant functional groups associated with the synthesis process. EDX analysis confirmed the incorporation of calcium, and SEM imaging revealed distinct irregular shapes of the nanoparticles with observable agglomeration. The investigation underscores the potential of calcium oxide nanoparticles (CaO NPs) derived from

mango leaf extract as effective antibacterial agents, presenting a promising strategy for medical applications in combating bacterial infections.

2.1.2: GREEN SYNTHESIS OF COPPER OXIDE NANOPARTICLES

Copper oxide (CuO) nanoparticles are distinguished by their significant antimicrobial, catalytic, and sensing characteristics. Various environmentally friendly synthesis methods have been explored, notably those utilizing plant extracts, including *Citrus limon* (lemon), *Moringa oleifera*, and the peel of Papaya. For example, Ahmed *et al*. (2018) reported the synthesis of CuO nanoparticles using *Citrus limon* peel extract, which facilitated rapid reduction and stabilization, yielding nanoparticles with average dimensions of 20-30 nm. The bioactive compounds present in these extracts, primarily flavonoids and polyphenols, are instrumental in reducing copper ions and mitigating particle agglomeration (Badawy *et al*., 2021). Additionally, the application of Moringa extracts has been shown to enhance the antimicrobial efficacy of CuO nanoparticles (Kalaiyan *et al*., 2021).

2.1.3: GREEN SYNTHESIS OF BINARY OXIDE NANOPARTICLES

Binary oxide nanoparticles, such as CaO-CuO composites, exhibit synergistic properties advantageous for catalysis and environmental applications. The green synthesis of such composites often involves co-precipitation or sol-gel processes assisted by plant extracts or microbial activity. For example, Singh *et al*. (2020) synthesized CaO-CuO binary nanoparticles using *Ocimum sanctum* (holy basil) leaf extract, which mediated the formation of uniform particles with enhanced photocatalytic activity for dye degradation. The phytochemicals in the extract served as a natural capping agent, controlling particle growth and preventing agglomeration.

Green synthesis offers a sustainable and eco-friendly approach to producing metal and binary oxide nanoparticles. The use of plant extracts not only reduces the reliance on hazardous chemicals but also introduces bioactive compounds that can enhance particle stability and functionality (Singh *et al*., 2020). Continued research exploring diverse biological sources and optimizing synthesis parameters can further improve the efficiency and applicability of green-synthesized CaO, CuO, and binary oxide nanoparticles.

2.2: GREEN SYNTHESIS OF METAL OXIDE NANOPARTICLE ONION PEEL EXTRACT

Onion (*Allium cepa* L.) has been esteemed for both its culinary and medicinal applications since ancient times. It ranks as the second most cultivated vegetable crop globally, following tomatoes, and is recognized across diverse cultures, being integrated into diets worldwide. This horticultural crop has a relatively short growth cycle and thrives in low-latitude regions. Often referred to as the "Queen of the Kitchen," the onion is highly regarded for its distinctive flavor, aromatic qualities, and unique taste, along with the medicinal properties attributed to its flavor compounds (Elattar *et al*., 2024). Onion (*A. cepa*) peel, a major agricultural waste product, is composed of total flavonoids, phenolic compounds, and volatile organic compounds (VOCs), with esters being the predominant constituent. These bioactive compounds contribute significantly to the therapeutic potential of onion peel extract (Chakraborty *et al*., 2022).

Recent investigations have demonstrated that the bioactivity of onion peel extract can be markedly enhanced when treated with various metal salts. In particular, the synthesis of nanoparticles derived from onion peel extract has garnered considerable interest for a multitude of applications. The development of hybrid nanoparticles, which involve the integration of onion peels with

metallic elements, has emerged as a promising area of research. These hybrid nanoparticles possess distinct properties and exhibit enhanced characteristics, including improved catalytic performance, greater stability, and unique optical or magnetic attributes. Such features render them highly adaptable for applications across diverse fields, including catalysis, sensing technologies, drug delivery systems, antimicrobial coatings, water purification, and environmental remediation (Puiso *et al*., 2023).

2.3: MECHANISM OF SYNTHESIS

The synthesis process typically involves a simple, one-pot reaction. Aqueous onion peel extract is mixed with precursor salts (e.g., $CaCl_2$ for CaO, $CuCl_2$ for CuO). The phytochemicals in the extract act as:

1. **Reducing Agents**: Bioactive compounds like quercetin and phenols donate electrons to reduce metal ions (Cu^{2+}) to their zero-valent states, which subsequently oxidize in solution to form metal oxide nuclei (Hanna *et al*., 2025; Moodi *et al*., 2021)

2. Capping and Stabilizing Agents: These compounds adsorb onto the surface of the nascent nanoparticles, preventing agglomeration and controlling particle growth, thereby determining the final size and morphology of the NPs (Ly *et al*., 2024). The resulting mixture is stirred, followed by washing, centrifugation, and calcination at moderate temperatures (e.g., 350-500 °C) to crystallize the amorphous product into pure metal oxide phases.

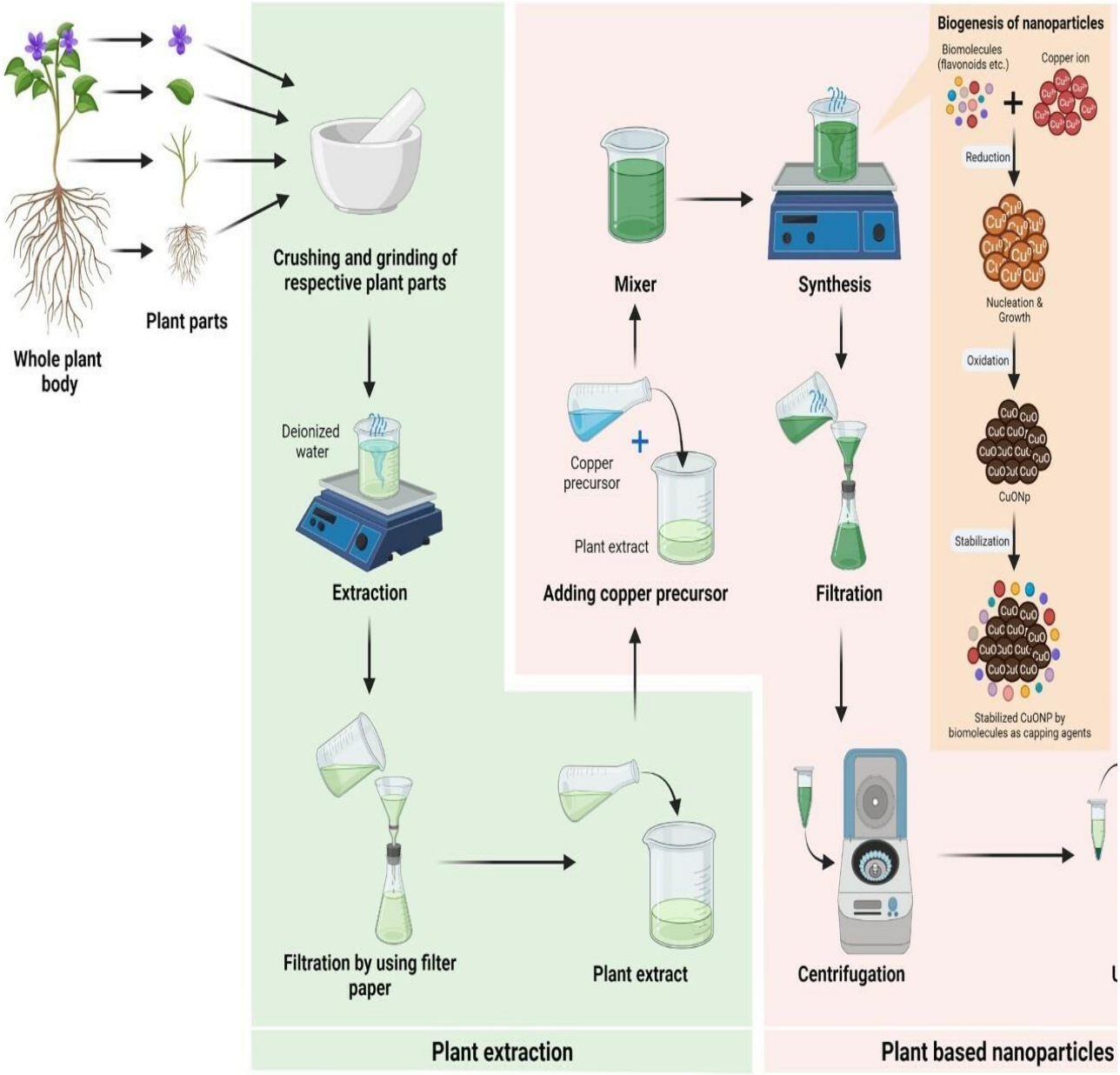

Plate 2.2: Biogenesis of nanoparticles (Chakraborty *et al*., 2022)

2.4: PHOTOCATALYTIC DEGRADATION OF PETROLEUM WASTEWATER

Photocatalytic degradation represents an advanced oxidation process employed for the degradation of pollutants characterized by high concentrations, intricate molecular structures, and low biodegradability. This process harnesses light energy to facilitate the breakdown of contaminants. The degradation mechanism involves the oxidation and hydrolysis of pollutant molecules, which is initiated by the absorption of photons across three distinct electromagnetic regions: visible (vis), ultraviolet (UV), and infrared (IR) (Raha and Ahmaruzzaman, 2022; Karthik *et al*., 2023).

When photocatalytic materials are activated by UV, visible, or infrared light, it triggers the migration of photo-responsive electrons from the valence band (VB) to the conduction band (CB), thereby generating pairs of photo-induced electrons and holes. The resultant electron-hole pairs subsequently interact with dioxygen, water, and hydroxyl groups, culminating in the production of reactive oxygen species (ROS), such as hydroxyl radicals (·OH) and superoxide radical anions (O_2·–). These reactive species engage with pollutant molecules, leading to either complete or partial degradation of persistent contaminants (Karthik *et al*., 2023).

The efficiency of photocatalytic degradation of petroleum hydrocarbons is contingent upon several factors, including light-harvesting efficiency, the effectiveness of the photogenerated electron-hole charge reactions, and the interactions between these charges and substrate molecules. The photodegradation process for petroleum hydrocarbons is facilitated when ultraviolet light interacts with the photocatalyst; photons possessing energy equal to or exceeding the band gap of the catalyst excite electrons from the valence band to the conduction band, generating positive holes (h+) within the valence band. The h+ then reacts with water molecules to yield hydroxyl radicals (·OH), while the excited electrons in the conduction band react with oxygen molecules to form

superoxide anion radicals ($O_2 \cdot -$). These highly reactive radicals are instrumental in the efficient degradation of organic dye molecules into simpler and smaller products such as water (H_2O) and carbon dioxide (CO_2) (Khan *et al*., 2023).

2.4.1: PHOTOCATALYTIC MECHANISM

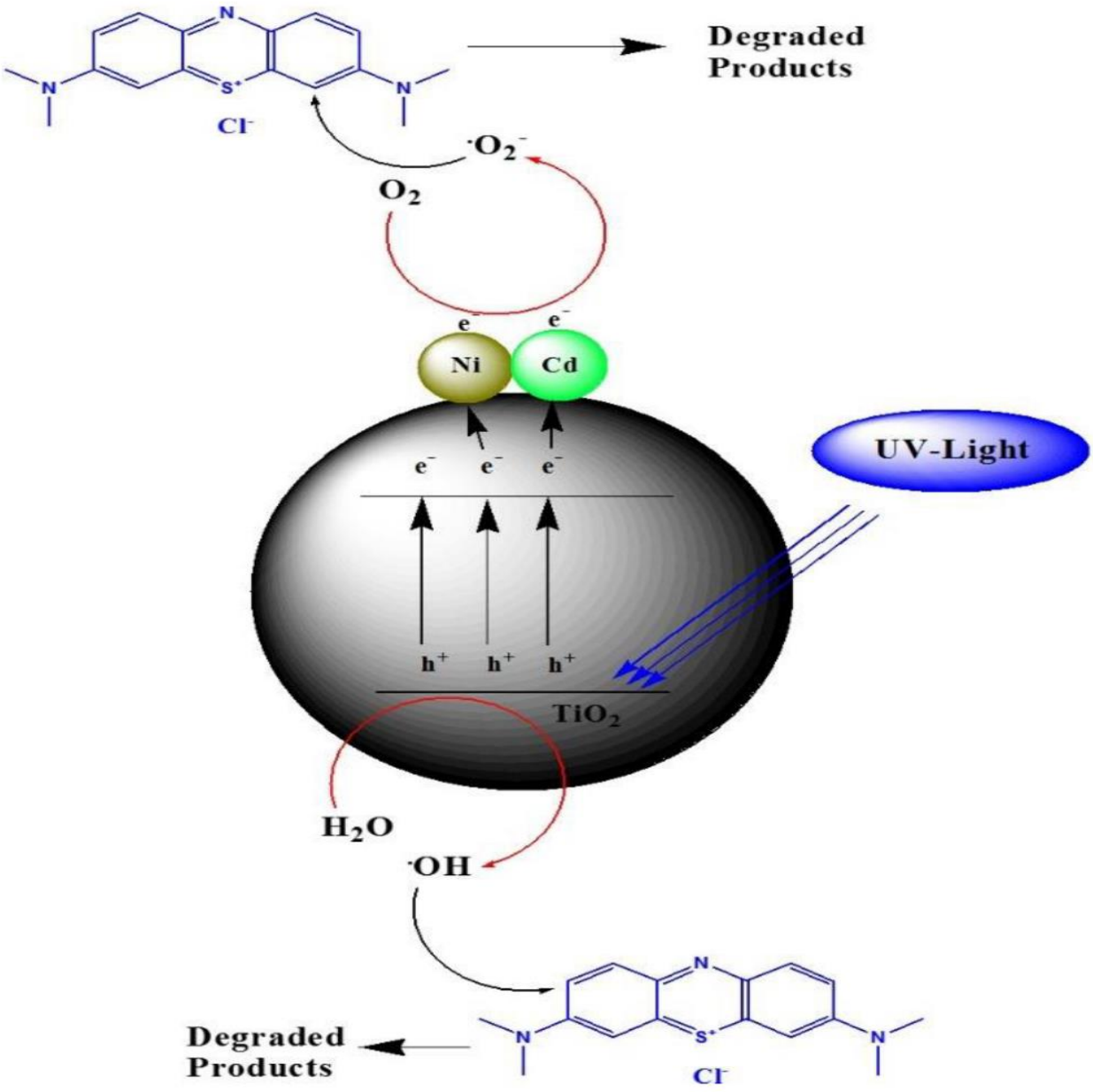

Figure 2.1: Mechanism of Photocatalysis. (Khan, *et al*., 2023)

Upon irradiation with light energy that meets or exceeds the effective bandgap of the CaO-CuO nanocomposite, electrons are excited from the valence band (VB) to the conduction band (CB), resulting in the formation of electron-hole pairs. The presence of a p-n heterojunction promotes the migration of electrons toward the CB of CaO, while holes are transferred to the VB of CuO. The excited electrons (e^-) engage with dissolved molecular oxygen (O_2) to yield superoxide radical anions ($O_2^{\bullet-}$). Concurrently, the photogenerated holes (h^+) can either directly oxidize organic contaminants or interact with water (H_2O) to produce highly reactive hydroxyl radicals (•OH). These reactive oxygen species (ROS), which include •OH and $O_2^{\bullet-}$, exhibit a non-selective reactivity that facilitates the breakdown of complex hydrocarbon chains, polycyclic aromatic hydrocarbons (PAHs), especially with conjugated bonds, and phenolic compounds present in petroleum wastewater into simpler and less toxic byproducts, as noted by Ahmed and Haider (2018). The role of CaO within this system is particularly significant; its robust basic sites can adsorb acidic constituents of wastewater, such as naphthenic acids. By concentrating these acidic components in proximity to the photocatalytic sites on CuO, CaO effectively enhances the rate of degradation of organic pollutants (Ahmed and Haider, 2018).

Research on green-synthesized nanocomposites indicates their considerable effectiveness in environmental applications. For example, a study conducted by Aklilu *et al.* (2022) investigated the degradation of methylene blue and 4 - nitrophenol, a model pollutant found in industrial wastewater, utilizing plant-mediated CuO-ZnO nanocomposites. The findings revealed an impressive degradation rate exceeding 95% under visible light within a 120-minute time, significantly surpassing the performance of pure CuO or CaO.

Further investigations into other binary systems, such as ZnO-CuO, have demonstrated that heterojunction formation results in enhanced charge separation. This enhancement is associated with a 2-3-fold increase in the degradation rates of dyes and organic acids compared to the performance of single oxide systems (Mahrsi *et al*., 2024).

Although direct research specifically addressing "onion peel-mediated CaO-CuO for petroleum wastewater" is still in its nascent stages, existing foundational studies provide compelling support for its potential. The organic compounds present in onion peel, which serve to cap the nanoparticles, may also play a critical role in enhancing both stability and dispersibility within the aqueous reaction medium, thereby further improving photocatalytic efficacy.

The green synthesis of CuO, and CaO-CuO binary nanoparticles using onion peel extract represents a paradigm shift towards sustainable nanotechnology. It effectively valorizes agricultural waste into a valuable resource for nanomaterial production. The resulting CaO-CuO nanocomposites, leveraging the synergistic effects of a p-n heterojunction, exhibit superior photocatalytic activity under visible light for the degradation of recalcitrant pollutants in petroleum wastewater. This approach aligns perfectly with the principles of green chemistry and circular economy. While challenges in scalability and application to real-world effluents persist, the existing body of literature provides a strong foundation for this technology, positioning it as a highly promising and environmentally benign solution for one of the industry's most pressing environmental problems.

CHAPTER THREE

MATERIALS AND METHODS

This chapter is divided into sections, viz, materials, which deal with all the reagents and apparatus used in the study, and methods, which deal with the scientific techniques employed in the study.

3.1: MATERIALS:

The various reagents and apparatus used in this study include the following

3.1.1: SAMPLES. The samples used in the study are onion (*A. cepa*) peel, and petroleum wastewater obtained from an oil company in Delta State, Nigeria. The grab method of sampling was used in the sampling of the petroleum wastewater.

3.1.2: REAGENTS

S/N	REAGENT	SOURCE	PROPERTIES
1.	Kjeldahl Catalyst	Lobachemiel, India	• **Physical State:** Typically supplied as solid, ready-to-use tablets or as a pre-weighed granular powder. • **Solubility:** Highly soluble in concentrated sulfuric acid and water (e.g., about 100 g/L in H_2O). • **Safety & Hazard:** Unmixed tablets containing selenium or high amounts of copper can be hazardous to the environment and cause severe eye/skin irritation. They require strict disposal protocols and should be stored in cool, dry places away from direct sunlight
2.	Conc.Sulphuric Acid	Sigma –Aldrich, Germany.	• **State & Appearance:** Clear, colorless, viscous, oily liquid. • **Molar Mass:** 98.079g/mol. • **Density:** 1.84g/cm^3 (heavier than water). • **Boiling Point:** 337^{o}C to 338^{o}C. • **Melting Point:** 10.37^{o}C (crystallizes into a solid just above typical room temperatures). • **Volscosity/Vapor Pressure:** Very high boiling point makes it relatively non-volatile.
3.	Phenol	Sigma –Aldrich, Germany.	• **Appearance:** Colorless to light pink crystalline solid at room temperature. It is deliquescent and can absorb enough moisture from the air to liquefy. • **Odor:** Distinctive sweet and medicinal smell. • **Melting Point:** 40.9° C. • **Boiling Point:** 181.8° C (relatively high due to strong intermolecular hydrogen bonding). • **Density:** 1.07 g/cm^3. • **Solubility:** Partially soluble in water (84.2 g/L at room temperature) but completely miscible at 65.9° C. Highly soluble in organic solvents like ethanol, ether, and chloroform.

4.	Sodium Potassium tartrate	Lolbachemie, India	• **Molecular Weight:** 282.22 g/mol • **Density:** 1.79 g/cm³ • **Melting Point:** 70°C – 80°C • **Solubility:** Highly soluble in water (526 mg/mL); slightly soluble in alcohol. • **pH Level:** 6.5 – 8.5. • **Hygroscopicity:** It is **deliquescent**, meaning it readily absorbs moisture from the air.
5.	Ammonium sulphate	Molychemie, India	• **Appearance:** Odorless, fine white crystals or granules. • **Density:** 1.77 g/cm³ • **Solubility:** Highly soluble in water (70.6 g per 100 ml of water at 0°C; 103.8 g at 100°C). It is insoluble in alcohol and acetone
6.	Sodium hydroxide	Sigma –Aldrich, Germany.	• **Appearance:** Colorless/white crystalline solid, commonly in pellets, flakes, or beads • **Molecular Weight:** 39.997 g/mol • **Melting Point:** 318ºC • **Boiling Point:** 1,388 ºC
7.	Sodium hypochlorite	Molychemie, India	• **Molecular Weight:** 74.44 g/mol • **Appearance:** Clear to pale greenish-yellow liquid • **Odor:** Strong, distinct chlorine-like smell • **Density:** 1.11 - 1.2 g/cm³ (depending on concentration) • **Solubility:** Completely miscible and soluble in water.
8.	Potassium nitrate	Sigma –Aldrich, Germany.	• **Appearance:** Colorless to white crystalline solid or powder • **Melting Point:** 334°C • **Boiling Point / Decomposition:** 400°C. • **Molecular Weight:** 101.10 g/mol
9.	Brucine Sulphate	Lobachemie, India	• **Molecular Formula:** $(C_{23}H_{26}N_2O_4)_2 \cdot H_2SO_4$ (often found as a heptahydrate) • **Molecular Weight:** 1013.13 g/mol (heptahydrate form) • **Appearance:** White to off-white crystalline powder • **Odor:** Odorless

			• **Melting Point:** Decomposes at approximately 180 °C to 185 °C before fully melting • **Solubility:** Highly soluble in water, ethanol, chloroform, and other organic solvents (which distinguishes it from the free-base brucine, which is poorly water-soluble) • **Optical Rotation:** -24 to -27° (c=1 in H_2O)
10.	Nitric Acid	Sigma –Aldrich, Germany.	• **State & Appearance**: Colorless liquid when pure, but often turns yellowish-brown over time due to photochemical decomposition (releasing dissolved NO_2). • **Density**: 1.51 g/cm^3 (heavier than water). • **Odor**: Pungent, acrid, and suffocating. • **Boiling Point**: 83°C (for 68–70% concentrated solutions). • **Melting Point**: 42°C. • **Solubility**: Completely miscible with water.
11.	Perchloric Acid	Sigma –Aldrich, Germany.	• **Chemical Formula:** $HClO_4$ • **Molecular Weight:** 100.46g/mol • **Appearance:** Colorless, oily, odorless liquid • **Density:** 1.768g/cm^3 • **Melting Point:** -17^{o}C (for 72% aqueous solution); -112 ^{o}C (anhydrous) • **Boiling Point:** 203^{o}C • **pKa Value:** -15.2±2.0 • **Solubility:** Highly miscible and soluble in water.
12.	Potassium dihydrogen phosphate	Sigma –Aldrich, Germany.	• **Appearance:** Odorless, colorless, transparent crystals or white crystalline powder. • **Density:** 2.338 g/cm³ • **Melting Point:** 252.6°C (decomposes upon further heating) • **Solubility:** Highly soluble in water (226 g/L at 20°C), but practically insoluble in organic solvents like ethanol

13.	Ammonium molybdate	Sigma –Aldrich, Germany.	• **Molecular Formula:** $(NH_4)_6Mo_7O_{24} \cdot 4H_2O$ (for the common tetrahydrate) • **Molecular Weight:** 1235.86 g/mol (for the tetrahydrate) • **Density:** 2.498 g/mL at 25 °C • **Melting/Decomposition Point:** Decomposes at approximately 190 °C • **Solubility:** Highly soluble in water (400 g/L at 20 °C), acids, and alkalis; insoluble in alcohol
14.	Antimony potassium tartrate	Sigma –Aldrich, Germany.	• **Formula:** $K_2Sb_2(C_4H_2O_6)_2 \cdot 3H_2O$ (trihydrate form) • **Molecular Weight:** 667.87 g/mol (trihydrate) • **Density:** 2.600 g/cm³ • **Melting Point:** Effloresces when exposed to air and decomposes at temperatures ≥ 300°C. • **Solubility:** Highly soluble in water (83 g/L at 20°C) and glycerol; insoluble in alcohol. • **pH:** An aqueous solution is slightly acidic.
15.	Corn Starch	Molychemie	• **Composition:** Primarily made of two polysaccharides: **amylose** (linear) and **amylopectin** (branched). Normal corn starch consists of roughly 25% amylose and 75% amylopectin. • **Solubility:** Insoluble in cold water but dispersible. • **Gelatinization:** When heated in water, granules absorb liquid, swell significantly, and form a translucent, viscous gel. Gelatinization typically occurs between 62°C and 72°C. • **Nutritional Value:** A highly concentrated carbohydrate containing about 381 kcal per 100 grams with virtually no protein or fat. • **pH & Stability:** Native corn starch is prone to breaking down under high shear force or acidic conditions, requiring modified variations for heavy processing.

16.	Hydrochloric acid	Sigma –Aldrich, Germany.	• **Acidity**: It is a strong acid that completely dissociates in water into \(H^{+}\) and \(Cl^{-}\) ions, yielding a pH near \(1\) for concentrated solutions. • **Reactivity**: Reacts strongly with most metals (producing flammable \(H_{2}\) gas) and metal oxides, while forming stable chloride complexes. • **Corrosiveness**: Highly corrosive to organic tissues and many materials, posing a severe risk of skin burns and eye damage. • **Volatility**: Concentrated solutions (about (36%))readily fume in air, releasing pungent hydrogen chloride gas. • **Chemical Formula**: (HCl(aq)\ • **Molar Mass**: 36.46g/mol • **Boiling Point**: 108.5 ^{o}C (varies by concentration) • **Melting Point**: -30^{o}C to -35^{o}C • **Density**: 1.18 g/cm^{3} at 25^{o}C • **Appearance**: Clear, colorless to slightly yellowish liquid
17.	Potassium dichromate	Molychemie	• **Formula & Molar Mass:** ($K_2Cr_2O_7$) |294.185g/mol • **Melting Point:** 398^{o}C (undergoes polymorphic transformation) • **Boiling Point:** 500^{o}C (decomposes upon boiling) • **Density:** 2.676 g/cm^{3} • **Solubility:** Moderately soluble in cold water; highly soluble in hot water. It is completely insoluble in alcohol and acetone
18.	Conc. Phosphoric acid	Sigma –Aldrich, Germany.	• **Molecular Weight:** 97.99 g/mol • **Density:** ~1.69 g/cm³ for the 85% solution (increases to 1.83–1.88 g/cm³ when pure/solid). • **Appearance:** Clear, colorless, syrupy liquid. • **Viscosity:** Highly viscous due to the extensive hydrogen bonding network. • **Melting Point:** 42.35°C for the pure, anhydrous form. Commercial 85%

			solutions remain liquid even at lower temperatures, solidifying around 21°C. • **Boiling Point:** Decomposes or boils at around 158°C, though concentrated solutions can reach up to 260°C depending on purity.
19.	Diphenylamine	Sigma –Aldrich, Germany.	• **Molecular Weight:** 169.22 g/mol • **Reactivity:** It is a very weak base. It can form water-soluble salts with strong acids. • **Sensitivity:** It is prone to discoloration when exposed to light or air, often turning yellow, tan, or brown due to oxidized impurities. • **Appearance:** Colorless to light-tan or brown crystalline solid • **Odor:** Pleasant, floral odor • **Melting Point:** 52°C to 54°C • **Boiling Point:** 302°C • **Density:** 1.16g/cm³ • **Solubility:** Nearly insoluble in water (approx 0.03 g per 100 mL), but readily dissolves in organic solvents such as alcohols, benzene, and acetone
20.	Hydrazine sulphate	Sigma –Aldrich, Germany.	• **APPEARANCE:** It is a white, odorless crystalline powder. • **Molecular Weight:** 130.12 g/mol • **Melting Point:** 254^{O}C (decomposes upon melting) • **Density:** 1.37g/cm^{3} at 20^{O}C • **Solubility:** Soluble in water (approx. 30g/L at 20^{O}C) and highly soluble in hot water; practically insoluble in ethanol and ether. • **pH:** Acidic; a 5% aqueous solution has a pH of approximately 1.3 to 1.5
21.	Hexamethylene tetramine	Molychemie, India	• **Molecular Weight:** 140.186 g/mol • **Appearance:** Odorless white crystalline powder or colorless crystals • **Density:** 1.33 g/cm³ at 20°C • **Melting Point:** Sublimes at 280°C without melting under normal atmospheric pressure • **Solubility:** Highly soluble in water (85g/100mL at 20°C) and soluble in

			polar solvents like methanol, ethanol, and chloroform. • **Aqueous Behavior:** Aqueous solutions are mildly basic, and exhibit inverse solubility (it becomes less soluble as the temperature increases)
22.	Ferrous ammonium sulphate	Molychemie, India	• **Chemical Formula:** $(NH_4)_2Fe(SO_4)_2 \cdot 6H_2O$ • **Molecular Weight:** 392.14 g/mol • **Appearance:** Pale green or blue-green monoclinic prismatic crystals • **Density:** 1.86 g/cm³ • **Solubility:** Highly soluble in water (approx. 26.9 g/100 mL at 20 °C); insoluble in ethanol and acetone. • **pH:** Forms a weakly acidic solution in water (pH 3–5). • **Melting/Decomposition Point:** Melts and decomposes into ammonia and nitrogen oxides above 100 °C
23.	Glucose D	Molychemie, India	• **Chemical Formula:** $C_6H_{12}O_6$ • **Molecular Weight:** 180.16 g/mol • **Physical State:** Odorless, white crystalline solid or powder • **Melting Point:** 146°C to 155°C (depending on the crystalline form) • **Solubility:** Highly soluble in water; dissolves endothermically, producing a cooling sensation • **Taste:** Sweet, about 70-80% as sweet as sucrose (table sugar). • **Optical Activity:** D-glucose is dextrorotatory, meaning it rotates plane-polarized light to the right. In aqueous solutions, it undergoes mutarotation.
24.	Sodium carbonate	Molychemie, India	• **Appearance**: White, odorless, hygroscopic powder or crystalline solid. • **Molecular Weight**: 105.99g/mol • **Melting Point**: 851^{O}C (Anhydrous). • **Density**: 2.54 g/cm3. • **Solubility**: Highly soluble in water; insoluble in acetone and ethanol.

			• **Alkalinity**: It is a strong base salt. When dissolved in water, it forms a highly alkaline solution (pH typically between 11 and 11.5 • **Reaction with Acids**: Neutralizes acids to form salt, water, and carbon dioxide.
25.	Buffer 4	Molychemie, India	• **Composition:** Contains a weak acid and its conjugate base (or its salt), allowing it to neutralize added hydroxide ions OH^- and hydrogen ions H^+. • **Calibration Standard:** Widely used as a primary calibration reference standard for standardizing **pH meters** and electrodes. • **Temperature Dependence:** Its exact pH can vary slightly with temperature changes. • **Buffer Capacity:** It performs best within the pH range of 3.0 to 5.0, with optimal buffering occurring right at its Pk_a value. • **Stability:** Maintains its pH well on standing, but is susceptible to mold growth if stored improperly over long periods.
26.	Buffer 7	Molychemie, India	• **Composition:** Typically formulated using a weak acid and its conjugate base, commonly a **Phosphate buffer** system (e.g., a mixture of monopotassium phosphate and disodium phosphate). • **pH Target:** Maintains a highly stable hydrogen ion concentration corresponding to (pH = 7.0) at a standard temperature (usually25^OC). • **pK_a:** The pK_a of the weak acid used in this buffer is typically close to 7.0 (e.g., phosphoric acid's second dissociation constant is roughly 7.2 at room temperature), allowing for optimal buffering capacity near neutrality. • **Neutrality:** The solution is considered chemically neutral, meaning the

			concentration of hydrogen ions H^+perfectly equals the concentration of hydroxide ions $[OH^-]$ at 1.0×10^{-7}M. • **Osmolarity & Ionic Strength:** Buffer solutions have specific ionic strengths and osmolarities designed not to interfere with biological assays or cellular environments.
27.	Buffer 9	Molychemie, India	• **pH Range:** Stays stable at exactly pH = 9.0 (±0.02, depending on the formulation). • **Composition:** Typically made by combining a weak base and its conjugate acid (e.g., an ammonia/ammonium chloride system or a boric acid/potassium chloride/sodium hydroxide system). • **Buffer Capacity:** Most effective within $pK_a \pm 1$ of the buffering agent. • **pH Stability:** The pH remains stable even when the solution sits for extended periods. • **Dilution Resistance:** Diluting the buffer with water has a negligible effect on the overall pH. • **Acid/Base Resistance:** Neutralizes added acids using its weak base component, and neutralizes added bases using its weak acid component. • **Temperature Sensitivity:** Like all buffers, the pH fluctuates slightly with temperature shifts.
28.	Potassium Chloride	Molychemie, India	• **Molar Mass**: 74.551g/mol • **Density**: $1.984 g/cm^3$ • **Melting Point**: 770^OC • **Boiling Point**: 420^OC • **Appearance**: Colorless to white crystals • **Taste**: Strong, slightly sour, saline taste. • **Solubility**: Highly soluble in water (253.9g/L at 20^OC), soluble in glycerol and alcohol, but insoluble in ether.

			• **pH**: Aqueous solutions are neutral, with a pH of approximately 7. • **Conductivity**: Dissolves readily in water to form solutions that are good conductors of electricity. • **Flame Color**: Produces a characteristic lilac or pale violet color when burned. • **Stability**: Chemically stable and non-volatile under standard ambient conditions.
29.	Phenolphthalein	Molychemie, India	• **Appearance**: Fine, white to yellowish-white crystalline powder. • **Odour**: Completely odourless. • **Density**: 1.277 g/cm^3 at 20^{O}C. • **Melting Point**: 258^{O}C to 263^{O}C. • **Solubility**: Highly soluble in alcohols (ethanol, ether) but poorly soluble in water. • **Chemical Properties** • **pH Indicator Range**: It changes color in the pH range of **8.2 to 10.0**. • **Stability**: Stable under standard laboratory conditions but sensitive to strong oxidizing agents.
30.	Silver Sulphate	Molychemie, India	• **Chemical Formula**: Ag_2SO_4 • **Molecular Weight**: 311.79 g/mol • **Density**: 5.45 g/cm³ • **Melting Point**: 652°C • **Boiling / Decomposition Point**: Decomposes at 1085°C • **Solubility**: Sparingly soluble in water (0.83 g/L at 25°C); insoluble in alcohol; soluble in sulfuric acid, nitric acid, and ammonium hydroxide. • **Reactivity**: Stable under normal conditions, but light-sensitive.
31.	Mercuric Sulphate	Molychemie, India	• **Molecular Formula**: $HgSO_4$ • **Molecular Weight**: 296.65 g/mol • **Density**: 6.47 g/cm³ (heavier than water) • **Decomposition Temperature**: Decomposes at 450°C into mercury vapor, sulfur dioxide, and oxygen.

		• **Solubility**: Insoluble in water (reacts/hydrolyzes), alcohol, acetone, and ammonia. Soluble in hydrochloric acid, hot dilute sulfuric acid, and sodium chloride solutions. • **Reactions**: Hydrolyzes in large amounts of water, breaking down into sulfuric acid and a yellow basic sulfate ($HgSO_4 \cdot 2HgO$). • **Toxicity**: Highly toxic through inhalation of fumes/dust, ingestion, or skin absorption. • **Health Effects**: Causes severe irritation to the eyes, skin, and respiratory tract. Prolonged or acute exposure can cause kidney damage, tissue lesions, and peripheral vascular collapse. • **Corrosivity**: Attacks metals like aluminum, copper, iron, and zinc in the presence of moisture.
32. Ascorbic acid	Molychemie, India	• **Molecular Formula:** $C_6H_8O_6$ • **Molar Mass:** 176.12 g/mol • **Appearance:** Odorless, white to pale yellow crystalline powder. • **Melting Point:** 190 to 192°C (decomposes upon melting). • **Solubility:** Highly soluble in water (330 g/L), moderately soluble in ethanol, and insoluble in chloroform and ether. • **Acidity (pK_a):** $pK_a1 = 4.2$, $pK_a2 = 11.6$. A 5% aqueous solution has an acidic pH of 2.2 to 2.5. • **Antioxidant Action:** It acts as an electron donor and reducing agent, neutralizing reactive oxygen species (ROS) and terminating oxidative chain reactions

3.1.3: APPARATUS/EQUIPMENT

1. Beakers
2. Conical flasks
3. Micropipette
4. Ambar bottles
5. Pipette (10ml)
6. Standard flask (100ml)
7. Standard flask (10ml)
8. Test tubes
9. Analytical Balance.
10. Oven
11. Furnace
12. Jenway pH meter
13. Conductivity meter
14. UV/Visible Spectrophotometer.
15. Atomic Absorption Spectrophotometer, AAS (Bulk Scientific)

3.2: METHODS.

3.2.1: PREPARATION OF SAMPLES:

The samples used in this study include the onion (A. cepa) peel and 'petroleum wastewater'.

The onion peels were obtained at the vegetable market, Upper Forestry Road, Benin City. They were washed with distilled water and air-dried for several days. The dried onion peel samples were pulverised and stored in clean, dried, airtight sample bottles.

The petroleum wastewater used in this study was obtained from an oil production company in Delta State, Nigeria. The grab method of sampling was employed in the sampling of the petroleum wastewater, stored in an amber bottle, and kept in the refrigerator. The pH, Temperature, electrical conductivity and dissolved oxygen of the water sample were measured on site using digital multimeter and dissolve oxygen meter.

3.2.2: EXTRACTION OF ONION PEEL

The method described by Otabor *et al*. (2025) was employed in the extraction of the onion peel with little modification. 10g of the ground sample was weighed into a 500ml flat-bottom flask. 100ml of distilled water was added and heated on a hot plate/stirrer at a temperature of 70 °C for one hour. Thereafter, the sample mixture was filtered with the aid of a filter paper, and the filtrates were stored in a sample bottle. The bottle was corked and kept in the refrigerator.

3.2.3: PHYTOCHEMICAL SCREENING OF ONION PEEL EXTRACT

The Phytochemical examinations of the plant extract were carried out using standard methods as employed by Tiwari *et al*. (2011), with little modification.

1. **Detection of Alkaloids:** This was done by first evaporating 2.0ml of the plant extract to dryness. Then the resultant residues were dissolved in 5ml of HCl (2mol/ dm^3) and filtered. The filtrate was divided into two test tubes. To the first test tube, a few drops of Mayer's reagent were added, and the formation of a yellow-coloured precipitate indicates the presence of alkaloids.

   The second test tube was treated with a few drops of Wagner's reagent, and the brownish-red precipitate formation indicates alkaloids.

2. **Detection of Glycoside:** This was done by dissolving 0.5 mg of the extract in about 1 ml of water and then aqueous NaOH solution was added. The formation of a yellow color indicates the presence of glycosides.
3. **Detection of Tannins:** To 1.0ml of the extract, 1.0ml of 1% gelatin solution containing sodium chloride was added. The formation of a white precipitate indicates the presence of tannins.
4. **Detection of Phenols:** This was done by treating 1.0ml of the plant extract with 4 drops of ferric chloride solution. The formation of a bluish-black colour indicates the presence of phenols.
5. **Detection of Saponins:** The foam test method and froth test methods were used in the detection of saponins. In the foam test method, 0.5g of the plant extract was shaken with 2.0 ml of distilled water. The formation of foam, which persists for 10 minutes, indicates the presence of saponins.

   In the froth test method, 5.0ml of the extract was diluted with distilled water to 20.0 mL, and this was shaken in a 50ml graduated cylinder for 15 minutes. The formation of a 1cm layer of foam indicates the presence of saponins.
6. **Detection of Flavonoids:** This was done using the alkaline reagent test and the lead acetate test. In the alkaline reagent test, the extract was treated with a few drops of a $2mol/dm^3$ solution of sodium hydroxide. The formation of an intense yellow colour, which becomes Colourless with the addition of dilute hydrochloric acid ($2mol/dm^3$), indicates the presence of flavonoids.

   In the lead test, the plant part extract was treated with a few drops of lead acetate solution. The formation of a yellow colour precipitate indicates the presence of flavonoids.

7. **Detection of Eugenols:** About 2ml of the extract was mixed with 5ml of 5% KOH solution. The aqueous layer was separated and filtered. A few drops of HCl were added to the filtrate. A pale-yellow precipitate was indicative of a positive test.
8. **Detection of Steroids**: 2 ml of acetic anhydride was added to 0.5 g of the extract of each with 2 ml of H_2SO_4. The colour changed from violet to blue or green in some samples indicating the presence of steroids.
9. **Detection of Terpenoid**: 0.2 g of the extract of the plant sample was mixed with 2 ml of chloroform ($CHCl_3$) and concentrated H_2SO_4 (3ml) was carefully added to form a layer. A reddish-brown colouration in the interface indicates positive results for the presence of terpenoids.
10. **Detection of Reducing Sugar:** This was done by dissolving 2ml of the plant extract in 2ml of water. The resultant solution was divided into two test tubes. The first test tube was treated with Benedict's reagent and then heated gently. Orange-red precipitate indicates the presence of reducing sugars.

    The second test tube was treated with 20 drops of boiling Fehling's solution (A and B). The formation of a brick–red precipitate in the bottom of the tube indicates the presence of reducing sugars.

3.2.4: SYNTHESIS OF CALCIUM OXIDE NANOPARTICLES

Calcium oxide nanoparticles were synthesized using the method described by Oghenefejiro *et al*. (2025) with modifications. In a 250 mL conical flask, 1.11g of $CaCl_2$ solution was mixed with 100 mL of onion peel extract prepared above and stirred at room temperature for 2 hours. Thereafter, a few drops of 0.1M solution of NaOH were added until the pH reached 10. The

mixture gradually formed a gray colloidal solution, indicating the formation of CaO nanoparticles. The resulting precipitate was obtained by centrifugation at 10,000rpm for 10 minutes, then washed with distilled water and 60% ethanol until a neutral pH was achieved. The precipitate was then oven-dried at 100℃ for 1 hour, and then casined in a muffle furnace at 450℃ for 2 hours, and then collected for characterization and application.

3.2.5: SYNTHESIS OF COPPER OXIDE NANOPARTICLE

The methods described by Oghenefejiro *et al*. (2025) and Padil and Cerník (2013), with modifications, were employed in the synthesis of copper oxide nanoparticles. In a 250ml conical flask. 1.705g of $CuCl_2 \cdot 2H_2O$ salt was dissolved in 100ml of onion peel extract prepared above and stirred at room temperature for 2 hours. Thereafter, a few drops of 0.1M solution of NaOH were added until the pH reached 10. The colour of the mixture gradually changed from blue to a bluish green, indicating the formation of CuO nanoparticles. The resulting precipitate was obtained by centrifugation at 10,000rpm for 10 minutes, then washed with distilled water and 60% ethanol until a neutral pH was achieved. The precipitate was then oven dried at 100℃ for 1hour, casined in a muffle furnace at 450℃ for 2hours, and then collected for characterisation and application.

3.2.6: SYNTHESIS OF CALCIUM OXIDE- COPPER OXIDE BINARY NANOPARTICLE

The binary nanoparticles of calcium oxide-copper oxide were prepared using the methods described by Urooj *et al* (2025) and Oghenefejiro *et al* (2025) with little modification. 1.11g of calcium chloride and 1.705g of copper chloride dihydrate were dissolved in 100 ml of onion peel extract and stirred at room temperature for 2 hours. Thereafter, a few drops of 0.1M solution of NaOH were added until the pH reached 10. The colour of the mixture gradually

changed to gray, indicating the formation of CaO – CuO binary nanoparticles. The resulting precipitate was obtained by centrifugation at 10,000rpm for 10 minutes, then washed with distilled water and 60% ethanol until a neutral pH was achieved. The precipitate was then oven dried at 100℃ for 1hour, casined in a muffle furnace at 450℃ for 2hours, and then collected for characterisation and application.

3.2.7: CHARACTERIZATION OF THE NANOCATALYSTS

The prepared nanocatalysts were subjected to characterization using the standard method described by Oghenefejiro *et al* (2025) with little modification.

1. X-Ray Diffraction (XRD)

X-ray diffraction analysis was employed to determine the crystalline phase, crystal structure, and average crystallite size of the synthesized nanoparticles. The powdered nanoparticle samples, obtained after calcination, were evenly packed into a standard sample holder. XRD analysis was performed using an X-ray diffractometer. The data were collected in the 2θ range of 10° to 80° with a step size of 0.02° and a counting time of 1 second per step. The resulting diffraction pattern was compared with standard reference patterns from the International Centre for Diffraction Data (ICDD) database for phase identification of the nanoparticles. The average crystallite sizes (D) were calculated from the full width at half maximum (FWHM, β) of the most intense diffraction peak using the Debye-Scherrer equation.

2. Fourier-Transform Infrared Spectroscopy (FTIR)

FTIR spectroscopy was utilised to identify the functional groups present on the surface of the nanoparticles and to confirm the role of onion peel extract as a reducing and capping agent. Approximately 1-2 mg of the dried nanoparticle powder was thoroughly mixed with 100 mg of anhydrous potassium bromide (KBr) and pressed into a transparent pellet using a hydraulic press under a pressure of 7-10 tons. The FTIR spectrum was recorded in transmission mode using an FTIR spectrometer (PerkinElmer Spectrum Two) over a wavenumber range of 4000 to 400 cm^{-1} with a resolution of 4 cm^{-1}. A background spectrum of a pure KBr pellet was collected and automatically subtracted from the sample spectrum. The characteristic absorption peaks were assigned to specific molecular vibrations (e.g., O-H stretch, C=O stretch, C-O stretch) of the phytochemicals from the onion peel extract, confirming their presence on the nanoparticle surface.

3. Dynamic Light Scattering (DLS) and Zeta Potential

DLS and Zeta Potential measurements were performed to determine the hydrodynamic diameter size distribution of the nanoparticles in suspension and their surface charge, which are critical indicators of colloidal stability. The nanoparticle powders were dispersed in deionized water to a final concentration of approximately 0.1 mg/mL. The suspensions were subjected to ultrasonication in a water bath for 30 minutes to ensure a monodisperse state and break down loose aggregates. Subsequently, 1 mL of the suspension was transferred into a disposable polystyrene cuvette (for DLS) and a folded capillary cell (for zeta potential). Measurements were carried out using a Zetasizer instrument (Malvern Panalytical Zetasizer Nano ZS) at a fixed temperature of 25°C. The hydrodynamic diameter and polydispersity index (PDI) were obtained from the DLS

measurement. The zeta potential was determined via Laser Doppler Velocimetry. The reported values represent the mean of three consecutive measurements.

4. Scanning Electron Microscopy/Energy-Dispersive X-ray Spectroscopy. (SEM-EDS)

SEM-EDS is an analytical technique that uses a scanning electron microscope to generate high-resolution images of a sample's surface and an EDS detector to determine its elemental composition simultaneously. This is achieved by bombarding the sample with an electron beam, which causes it to emit X-rays at specific energies that identify the elements present.

Scanning Electron Microscopy was utilized to investigate the surface morphology, primary particle size, and agglomeration state of the nanoparticles. Dilute suspensions of the nanoparticles in deionized water were prepared via ultrasonication for 15 minutes. Single drops of the suspension were deposited onto cleaned aluminium stubs and allowed to air-dry under ambient conditions. The dried samples were subsequently sputter-coated with thin layers (approximately 10-15 nm) of gold to enhance surface conductivity. The coated sample was then transferred to the chamber of the SEM. Imaging was performed at an accelerating voltage of 15-20 kV under high vacuum mode. Multiple micrographs were captured at various magnifications (e.g. 50,000x to 100,000x) from different regions of the sample to ensure representative analysis. The electrons emitted from the samples were captured by the EDS detector, which identifies and quantifies the various elements present in the samples.

3.2.8: PHYSICOCHEMICAL CHARACTERIZATION OF PETROLEUM WASTEWATER

All physicochemical characterization of the petroleum wastewater used in the study was done using the standard methods for water analysis as described by Ademoroti (1996). The analysis was done in triplicate.

3.2.8.1: DETERMINATION OF TURBIDITY

2ml of distilled water was poured into the cuvette and read at zero in the spectrophotometer at 450nm. Thereafter, 2ml of the water sample was also poured into another cuvette, and absorbance was measured at 450nm and recorded. The Working Standards were subjected to similar treatment.

Calculation

Turbidity (NTU) = Instrument Reading x Slope Recip.

3.2.8.2: DETERMINATION OF SUSPENDED SOLIDS

Whatman Filter Paper No. 1 was dried in the oven at 105℃, to constant weight (X_1g). Then 100ml of water sample was passed through the filter paper in a funnel, into a conical flask. Thereafter, the filter paper was dried in the oven at 105℃ to a constant weight. The weight of the filter paper with its content (X_2g) was recorded.

Calculation

Weight of Suspended solids=(X_2-X_1)g

Suspended solids (mg/l) = (X_2-X_1) × 1000 ÷ volume of sample

3.2.8.3: TOTAL DISSOLVED SOLID (TDS)

This was extrapolated from the Electrical conductivity using the mathematical relationship:

$TDS = EC \times 0.55$

3.2.8.4: TOTAL SOLID

This was obtained by summing the Total Suspended Solid and Total Dissolved Solids.

TS (mg/L)= TSS + TDS

3.2.8.5: NITRATE NITROGEN.

10ml of the filtered water sample was transferred into a 50ml flask. Then 2ml of brucine was added and rapidly followed by the addition of 10mL conc. H_2SO_4. This solution was properly mixed and allowed to stand for 10 minutes, after which it was made up to the 50ml mark with distilled water. The standard solutions, which were prepared from Potassium nitrate, were also treated same way. The absorbance of the sample solution and standard solutions were measured with the aid of the UV/Visible Spectrophotometer, at 470nm.

CALCULATION

$$NO_3 - N \text{ (PPM)} = \frac{\text{instrument reading} \times \text{slope reciprocal} \times \text{colour volume}}{\text{aliquout taken}}$$

3.2.8.6: DETERMINATION OF PHOSPHORUS.

The ascorbic acid colour development method, as reported by Dmitrievich (2013), was used. 10ml of the sample was placed in a Kjeldahl flask. 10ml of mixed acid (Nitric acid and perchloric acid mixture, ratio 3 to 1) was added to the flask. The flask and its content were mildly heated for about 20 minutes at a temperature of 40 °C and then increased to about 100 °C for another 20 minutes. The sample was allowed to cool, about 20 mL of distilled water was added and filtered into a standard flask. It was made up to the 100ml mark with distilled water.

Phosphorous working standard solutions of 2,4,6,8 and 10ppm are prepared by pipetting 2,4,6,8 and 10ml of the 100ppm standard into 100ml respective already labelled standard flasks and made up to mark with distilled water.

From each standard solution, 1ml was pipetted out and placed in the respective labelled round-bottom flask. 1ml from the digested samples was also placed in an appropriately labelled round-bottom flask, and to each of the round-bottom flasks, 8ml of distilled water was added. This was followed by the addition of 1ml phosphorous colouring reagent (which was prepared using 100ml of 5N Sulfuric acid H_2SO_4, 30ml of ammonium molybdate solution and 10ml of antimony potassium tartrate solution. The content of the flask was swirled gently to ensure proper mixing. Then 0.5ml of the ascorbic acid solution was added to the flasks. The absorbance of the mixtures was read at 880 nm using a UV/VIS spectrometer.

$$\text{PHOSPHOROUS} = \frac{\text{instrument reading} \times \text{slope reciprocal} \times \text{colour volume} \times \text{digested volume}}{\text{aliquout taken} \times \text{sample volum}}$$

PHOSPHATE

The phosphate value of the sample was calculated from the value of Total phosphorus.

Using the formula, **Total phosphorus × 2.29 =PHOSPHATE**

3.2.8.7: DETERMINATION OF SULPHATE.

The determination of sulphate content of the sample was done by the method reported by C.M.A. Ademoroti (1996).

10 mL of the sample digest was placed in a 100 mL flat-bottom flask. This was followed by the addition of 1ml of 6N Hydrochloric acid (HCL), 0.5ml of $Bacl_2$ and 1ml of starch solution, shaken,

and left to stand for about 5 minutes. Standard solutions of sulphate and blank digest were also treated same manner. Their absorbances were measured at 420nm using a UV/vis spectrometer.

$$\text{SULPHATE} = \frac{\text{instrument reading} \times \text{slope reciprocal} \times \text{colour volume} \times \text{digested volume}}{\text{aliquout taken} \times \text{sample volume}}$$

3.2.8.8: BIOCHEMICAL OXYGEN DEMAND (5 DAYS, 27°C)

The Biological Oxygen Demand (BOD) was determined following the standardized methodology established by Ademoroti (1996). Initially, the water sample was prepared by saturating it with air using a water aerator in a partially filled bottle. Subsequently, the aerated water sample was inoculated with supernatant obtained from domestic wastewater after a settling period of one hour. Following the inoculation, the Dissolved Oxygen (DO) of the sample was immediately measured using a calibrated DO meter, with the resulting value recorded as DO1. The sample container was then securely sealed and placed in an incubator for a duration of five days.

On the fifth day, the Dissolved Oxygen of the sample was again measured using the calibrated DO meter, and this value was recorded as DO5. The Biological Oxygen Demand (BOD) of the water sample was calculated utilizing the following equation:

$$BOD = DO1 - DO5._5$$

3.2.8.9: CHEMICAL OXYGEN DEMAND (COD)

The COD of the sample was also carried out using the standard colourimetric method as described by Ademoroti (1996) with modifications. 2.0 mL of the water sample was measured into a cleaned, dried 20ml capped culture tube. To this, 0.04 g of mercuric sulfate and 1.0 mL of a 0.125 M potassium dichromate ($K_2C_{r2}O_7$) solution were added, followed by thorough mixing. Thereafter, 3.0 mL of Sulphuric acid – Silver Sulphate reagent was added gradually, with swirling and mixing of contents. The tube was then capped and heated on a HACH digester for

two hours at 150 °C. Standard COD solutions prepared from glucose were also subjected to the same treatment. Reagent blank digestion was also done. After two hours, the digester was turned off and the tubes were allowed to cool. The absorbance of the reagent blank, standards and sample was read at 585nm. The COD of the sample calculated from the calibration curve of the standard solutions.

3.2.8.10: DETERMINATION OF CHLORIDE

100 ml of the sample was measured in a conical flask. This was followed by the addition of 1 mL K_2CrO_4 indicator solution, and the resultant solution was titrated with 0.0141N $AgNO_3$ titrant to a pinkish-yellow endpoint.

Blank titration was carried out with a distilled water blank.

Calculation

$$mgCl^-/L = \frac{(A-B) \times N \times 35.450}{\text{volume of sample}}$$

where:

A =mL titration for the sample

B =mL titration for blank

N = normality of $AgNO_3$

3.2.8.11: TOTAL ORGANIC CARBON.

The standard procedure detailed by C.M.A. Ademoroti (1996) was employed to determine the total organic carbon content. Initially, 1 gram of the sample was placed into a 500 mL conical flask. Following this, 10 ml of potassium dichromate solution was carefully added using a pipette, followed by the addition of 20 ml of concentrated sulfuric acid. The flask was subsequently swirled

to ensure thorough mixing and allowed to stand for 30 minutes. After this period, 200 ml of distilled water and 10 ml of concentrated phosphoric acid were introduced, and the flask was allowed to cool.

A blank was prepared similarly, using 10 ml of potassium dichromate and 20 ml of concentrated sulfuric acid, which also stood for 30 minutes. To this mixture, 200 ml of distilled water and 10 ml of concentrated phosphoric acid were added in a 500 ml beaker.

For both the sample and blank solutions, 11 drops of a diphenylamine indicator—previously prepared by dissolving 1 gram of diphenylamine in 100 ml of concentrated sulfuric acid—were added and stirred. The solutions were then titrated with ferrous ammonium sulfate until a green colour endpoint was achieved. The total organic carbon was calculated using the formula:

$$\frac{(\mathbf{Vblank - Vsample}) \times 0.3 \times 0.5 \times 10000}{\mathbf{weight} \div 1000} \times 1.334 = \textbf{Total organic carbon}$$

3.2.8.12: WET ASHING FOR HEAVY METAL ANALYSIS

The methodology employed was based on the procedure outlined by Victor Dmitrievich (2013). A 10 g sample was placed into a Kjeldahl flask, followed by the addition of 10 mL of a mixed acid solution consisting of nitric acid and perchloric acid in a 3:1 ratio. The flask and its contents were subjected to mild heating for approximately 20 minutes at a temperature of 40 °C, which was subsequently increased to around 100 °C for an additional 20 minutes. Following the heating phase, the sample was allowed to cool. Subsequently, about 20 mL of distilled water was added, and the mixture was filtered into a standard volumetric flask. The final volume was adjusted to the 100 mL mark with distilled water.

3.2.8.13: HEAVY METAL ANALYSIS

The heavy metals of interest in this study were assayed using an Atomic Absorption Spectrophotometer.

3.2.9: PHOTOCATALYTIC DEGRADATION STUDY.

The study of photocatalytic degradation in petroleum wastewater was conducted in accordance with the methodology established by J. Saien and H. Nejati (2007) with modifications. 250 mL of the petroleum wastewater sample containing a predetermined concentration of Chemical Oxygen Demand (COD) was transferred to a 500ml Erlenmeyer flask, with a specified amount of catalyst added. The solution was subjected to continuous circulation and exposure to sunlight irradiation. Typical reaction runs varied in reaction conditions such as catalyst dosage, pH and temperature. At regular intervals of 30 minutes, samples of 10 mL were collected and subjected to centrifugation to facilitate the separation of the nanocatalysts. COD levels were quantitatively assessed using the standard colourimetric methods, discussed above and the percentage COD reduction (R) calculated using the formula:

$$\mathrm{R} = (\mathrm{COD1} - \mathrm{COD2}) \div \mathrm{COD1} \times 100$$

Where COD1 = COD of the sample before treatment

COD2 = COD of the sample after treatment

3.2.9.1: EFFECT OF CATALYST DOSE

The effect of the catalyst dose on the photocatalytic degradation of the petroleum wastewater was studied by varying the catalyst weight (0.125g, 0.100g, 0.075g, 0.05g, and 0.025g), which was dosed into a 250 mL portion of the petroleum wastewater. The reactor temperature, contact time, and the pH of the petroleum wastewater were kept constant. The reaction was then subjected to the same conditions as above.

3.3.9.2: EFFECT OF CONTACT TIME

The effect of the catalyst's contact time with the petroleum wastewater was studied by measuring 250 mL of the petroleum wastewater into the reaction flask. Then the optimum dose was added, maintaining the pH of the petroleum wastewater and the temperature at 30℃ in a water bath. The reaction was exposed to sunlight while shaking the reactor intermittently to ensure proper distribution of the catalyst in the reaction mixture. Samples were collected every 30 minutes for centrifugation and COD analysis to determine the time that yielded the highest percentage reduction in COD.

3.2.9.3: EFFECT OF pH

The effect of pH of the petroleum wastewater on the photocatalytic degradation study was done by adjusting the pH with a 0.1M solution of NaOH for a basic pH and a 0.1M solution of HCl for an acidic pH. 250mL of the petroleum wastewater with a pH of 2 was placed in a 500mL Erlenmeyer flask. The optimum catalyst dose was added, and the temperature was adjusted to the optimal value. The reaction was then exposed to sunlight irradiation for an optimum time. The experiment was then allowed to proceed as above. This process was repeated for petroleum wastewater with pH 4, pH 6, pH 8, and pH 10.0.

3.2.9.4: TREATMENT OF PETROLEUM WASTEWATER WITH THE OPTIMUM CONDITION

The optimum conditions established in the above experiments for the three different nanoparticles were then used to treat the petroleum wastewater, and the treated water was subjected to physicochemical analysis to compare the efficiency of the nanocatalysts.

CHAPTER FOUR

RESULT

This chapter is divided into two sections, viz., Results, which present the results obtained from the study, and Discussion, which attempts to interpret these results.

4.1: RESULT

The results obtained from this study are presented in the tables and figures below:

Table 4.1: The Result of the Phytochemical Screening of the onion Extract

S/N	PARAMETERS	TEST METHOD	OBSERVATION
1	Glycosides	General Test	+
2	Saponins	Frothing	+
3	Alkaloids	Picric acid/Wagner	+
4	Phenolics	Ethanol/$FeCl_3$	+
5	Eugenols	KOH/HCl	+
6	Steroids	Acetic Anhydride/H_2SO_4	-
7	Terpenoids	Salkowski Test	+
8	Flavonoid	Lead Acetate	+
9	Tannins	$FeCl_3$	+
10	Reducing Sugar	Fehling Solution A&B	-

KEY:
+ = Present; - = Absent

Table 4.2: The Result of Physicochemical Characterisation of the petroleum wastewater before treatment.

S/N	PARAMETERS	PEWW1	PEWW2	PEWW3	SEM
1	Ph	8.34	8.40	8.37	8.37±0.02
2	Electrical conductivity (µs/cm)	642	650	645	645.67±2.33
3	Total Dissolved Solids (mg/L)	353.10	357.50	354.75	355.12±1.28
4	Temperature (^{o}C)	24.4	24.4	24.5	24.43±0.03
5	Total Suspended Solids (mg/L)	2.60	2.40	2.20	2.40±0.12
6	Total Solids (mg/L)	355.7	359.9	356.95	357.52±1.25
7	Chloride (mg/L)	246.14	241.82	238.96	242.31±2.09
8	Dissolved Oxygen (mg/L)	3.40	3.20	3.30	3.30±0.06
9	Biological Oxygen Demand(mg/L)	17.80	16.90	16.90	17.20±0.30
10	Chemical Oxygen Demand (mg/L)	2564.31	2298.79	2317.58	2393.56±85.59
11	Phosphate (mg/L)	19.28	20.14	18.58	19.32±0.46
12	Sulphate (mg/L)	27.43	26.97	27.94	27.45±0.28
13	Nitrate (mg/L)	91.88	87.94	88.76	89.53±1.20
14	Total Hydrocarbon (mg/L)	1372.34	1321.67	1367.45	1357.15±18.28
15	Turbidity (NTU)	798.41	802.50	789.00	796.64±0.53
16	Total Organic Carbon (mg/L)	10.54	9.96	8.73	9.74±0.53
17	Cadmium (mg/L)	0.10	0.08	0.08	0.09±0.01
18	Lead (mg/L)	0.10	0.10	0.20	0.13±0.03
19	Nickel (mg/L)	0.32	0.31	0.31	0.31±0.003
20	Copper(mg/L)	0.50	0.54	0.53	0/52±0.01
21	Iron (mg/L)	10.10	10.00	10.00	10.03±0.03

KEY

PEWW = Untreated petroleum wastewater

SEM = Standard error of mean

4.2: THE RESULTS FOR THE CHARACTERIZATION OF THE PHOTOCATALYST

Results

			Size (d.nm...	% Intensity:	St Dev (d.n...
Z-Average (d.nm):	45.82	Peak 1:	23.74	79.9	6.784
PdI:	0.193	Peak 2:	279.7	15.2	80.00
Intercept:	0.635	Peak 3:	5154	4.9	514.6
Result quality	Refer to quality report				

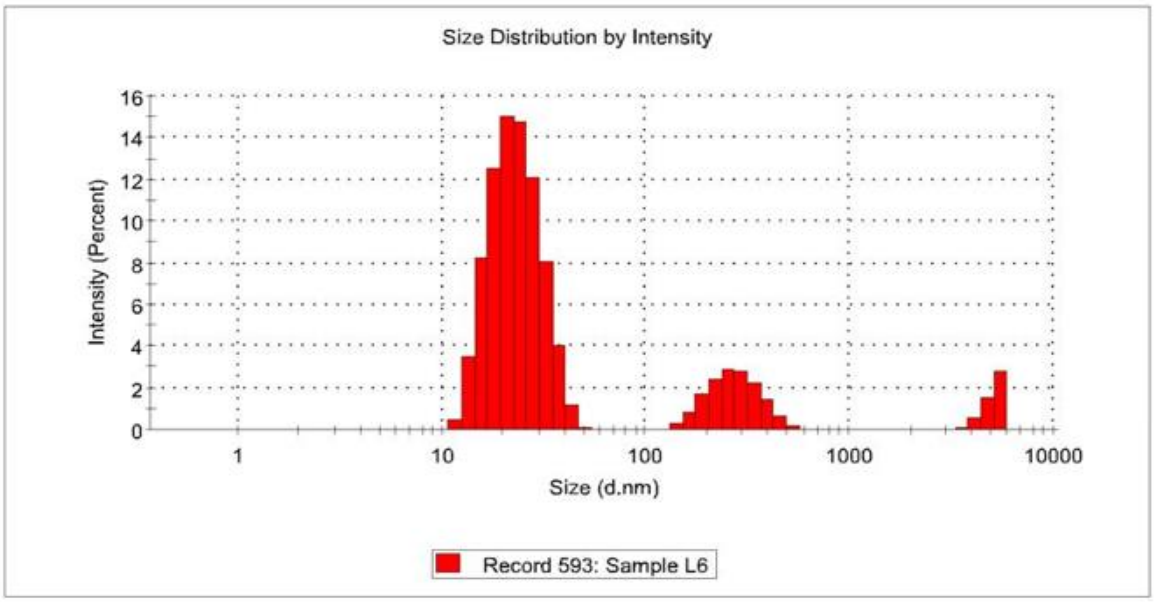

Figure 4.1: Dynamic Light Scattering (DLS) analysis for CuO nanoparticles

Results

			Size (d.nm...	% Intensity:	St Dev (d.n...
Z-Average (d.nm):	20.63	Peak 1:	15.68	69.6	4.623
PdI:	0.405	Peak 2:	224.5	30.4	84.96
Intercept:	0.954	Peak 3:	0.000	0.0	0.000
Result quality	Good				

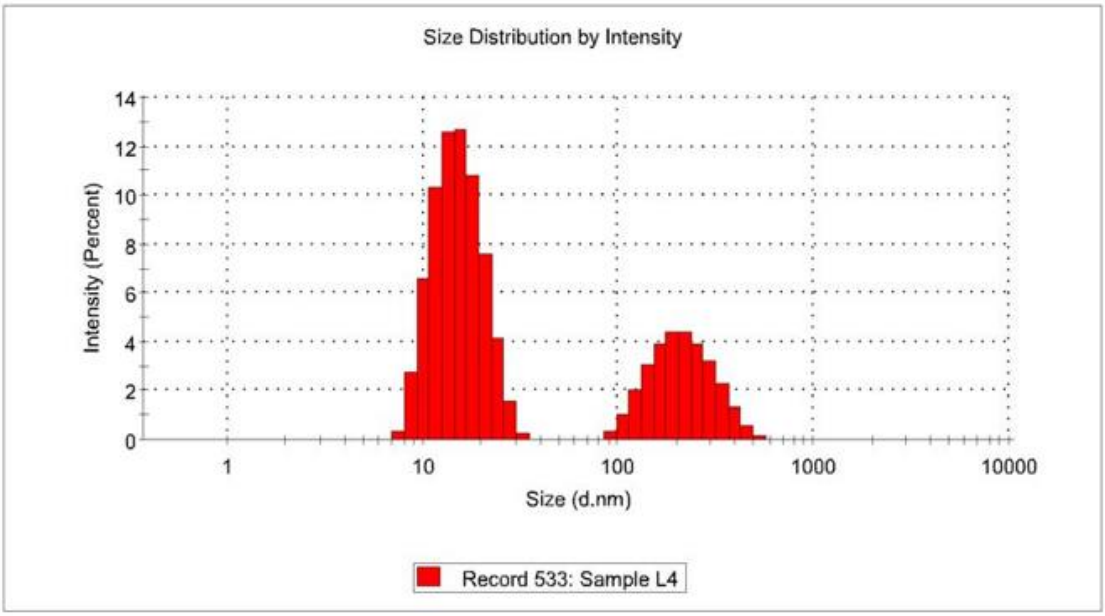

Figure 4.2: Dynamic Light Scattering (DLS) analysis for CaO – CuO binary nanoparticles.

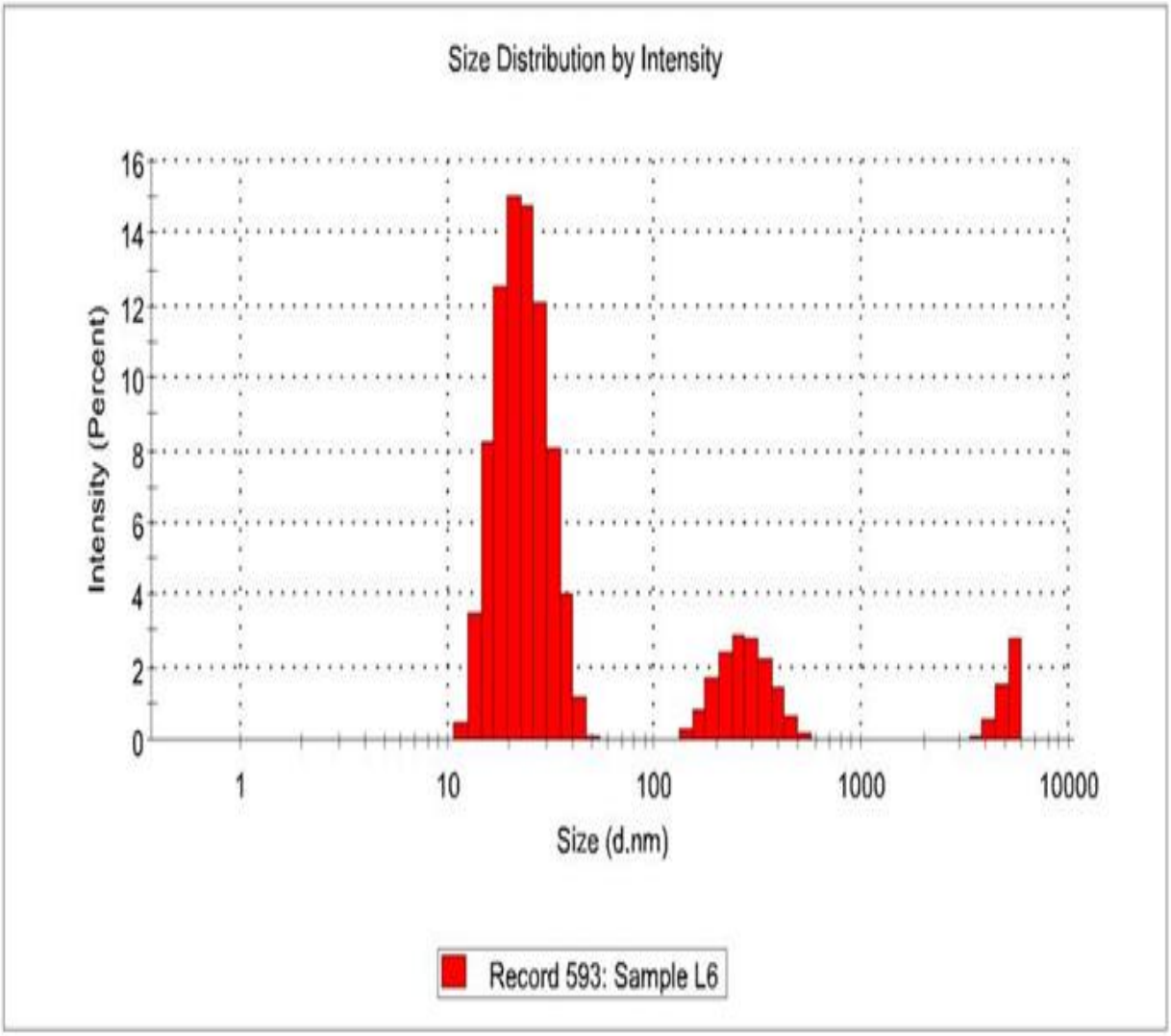

Figure 4.3: Dynamic Light Scattering (DLS) analysis for CaO nanoparticles.

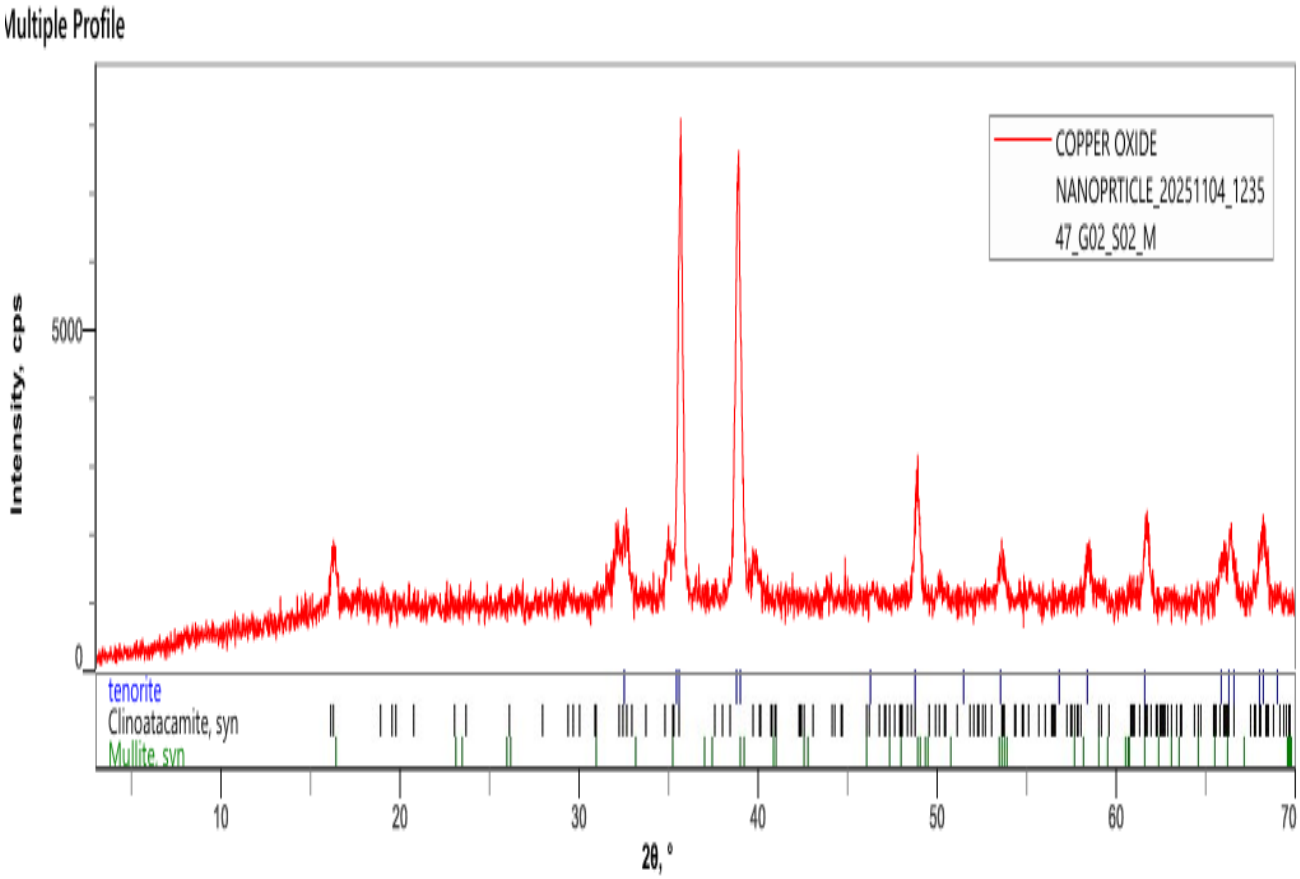

Figure 4.4: X-ray Diffraction analysis for CuO nanoparticles

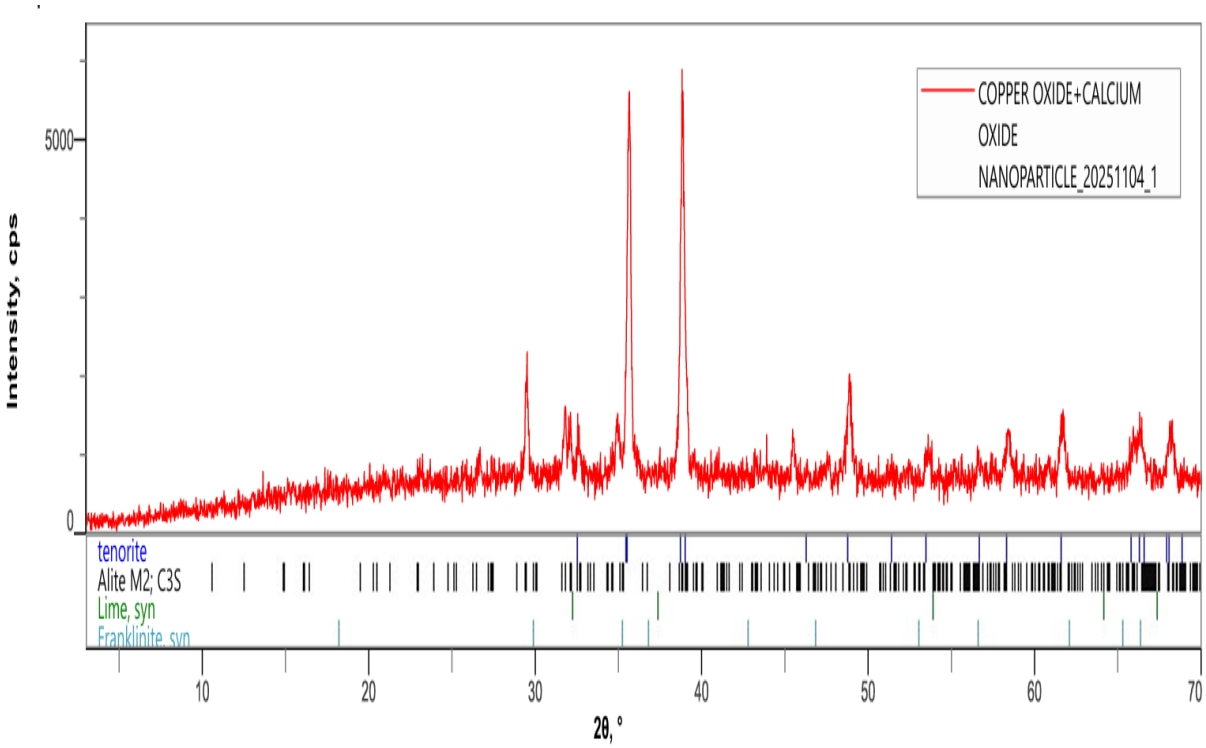

Figure 4.5: X-ray Diffraction analysis for CaO- CuO binary nanoparticles

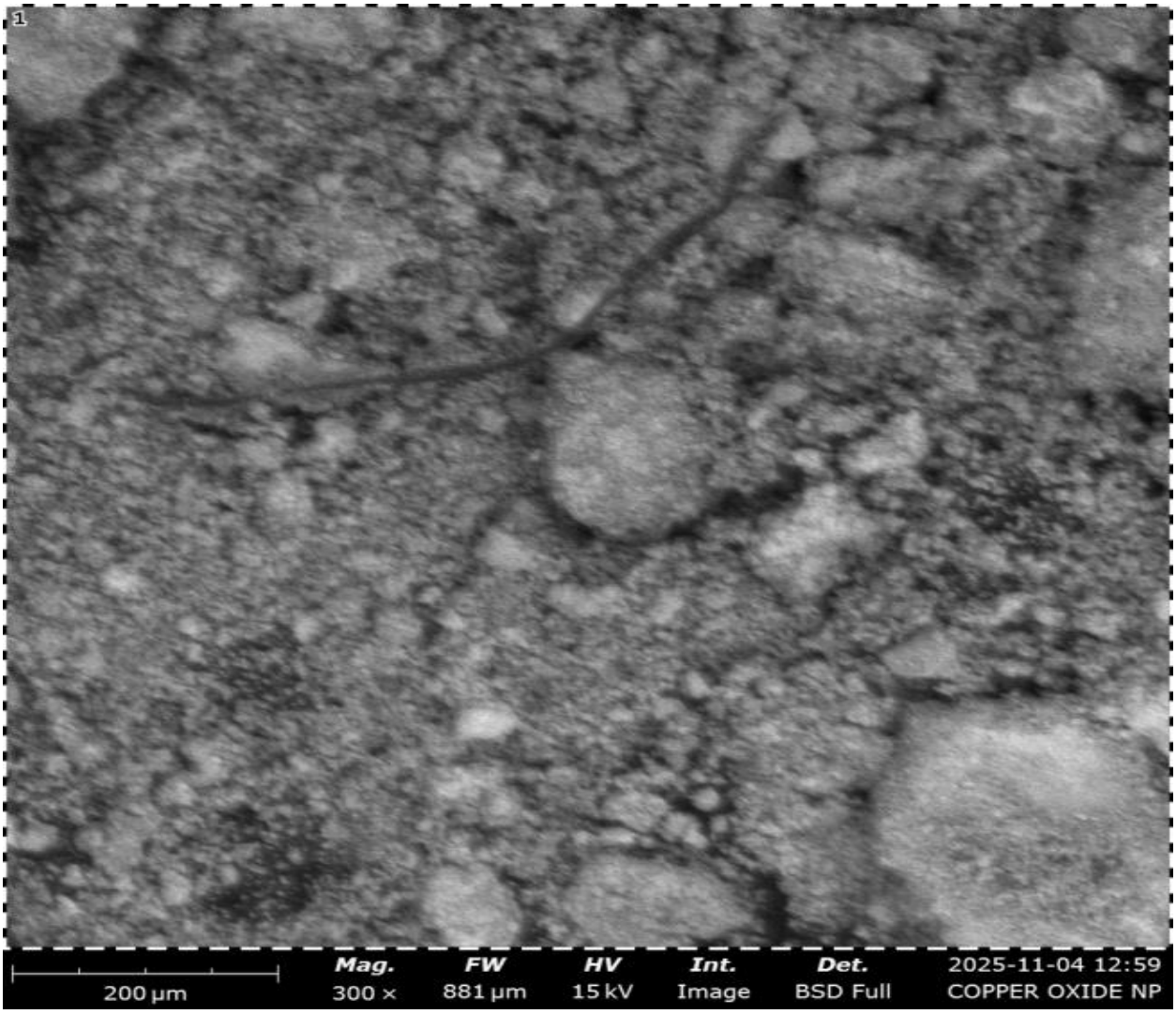

Figure 4.6: Scanning Electron Microscope (SEM) analysis of CuO nanoparticles

Table 4.3: A table showing the result of the Energy Dispersive X-ray Spectroscopy (EDX) analysis of CuO nanoparticle

Element Number	Element Symbol	Element Name	Atomic Conc.	Weight Conc.
29	Cu	Copper	77.81	88.73
17	Cl	Chlorine	5.70	3.63
6	C	Carbon	7.43	1.60
14	Si	Silicon	2.93	1.48
26	Fe	Iron	1.25	1.25
13	Al	Aluminum	2.11	1.02
56	Ba	Barium	0.34	0.83
11	Na	Sodium	1.00	0.41
28	Ni	Nickel	0.37	0.39
20	Ca	Calcium	0.40	0.29
19	K	Potassium	0.30	0.21
12	Mg	Magnesium	0.36	0.16
22	Ti	Titanium	0.00	0.00
40	Zr	Zirconium	0.00	0.00
25	Mn	Manganese	0.00	0.00
24	Cr	Chromium	0.00	0.00
15	P	Phosphorus	0.00	0.00
16	S	Sulfur	0.00	0.00
47	Ag	Silver	0.00	0.00
50	Sn	Tin	0.00	0.00

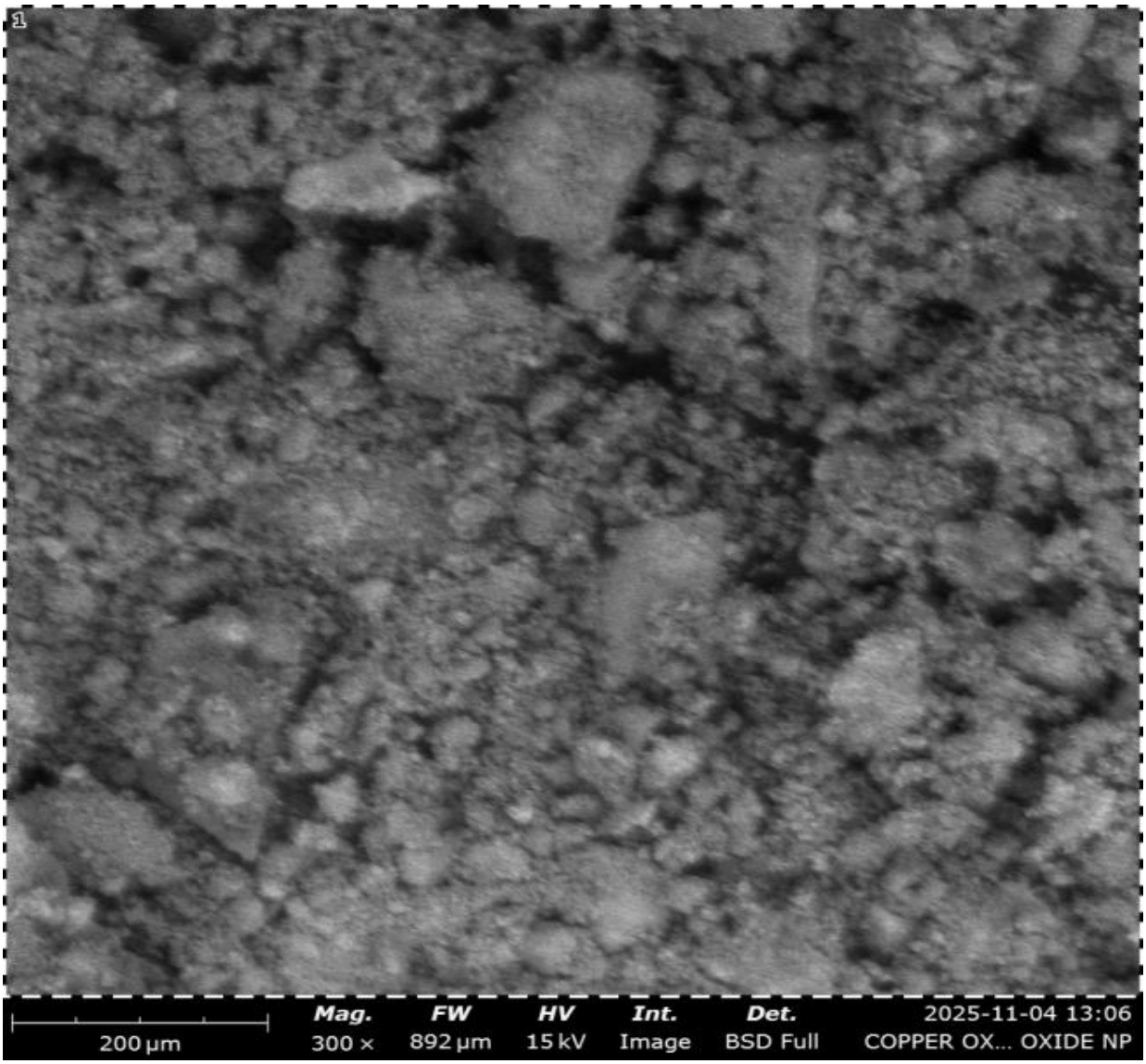

Figure 4.7: Scanning Electron Microscope (SEM) analysis of CaO- CuO binary nanoparticles

Table 4.4: A table showing the result of the Energy Dispersive X-ray Spectroscopy (EDX) analysis of CaO-CuO binary nanoparticle

Element Number	Element Symbol	Element Name	Atomic Conc.	Weight Conc.
29	Cu	Copper	53.81	69.12
20	Ca	Calcium	19.35	15.67
17	Cl	Chlorine	9.64	6.91
6	C	Carbon	8.54	2.07
11	Na	Sodium	3.07	1.43
14	Si	Silicon	1.73	0.98
47	Ag	Silver	0.27	0.60
16	S	Sulfur	0.89	0.58
50	Sn	Tin	0.21	0.50
19	K	Potassium	0.59	0.47
28	Ni	Nickel	0.39	0.46
26	Fe	Iron	0.39	0.44
13	Al	Aluminium	0.56	0.30
24	Cr	Chromium	0.25	0.27
15	P	Phosphorus	0.33	0.20
40	Zr	Zirconium	0.00	0.00
12	Mg	Magnesium	0.00	0.00
56	Ba	Barium	0.00	0.00
22	Ti	Titanium	0.00	0.00
25	Mn	Manganese	0.00	0.00
30	Zn	Zinc	0.00	0.00

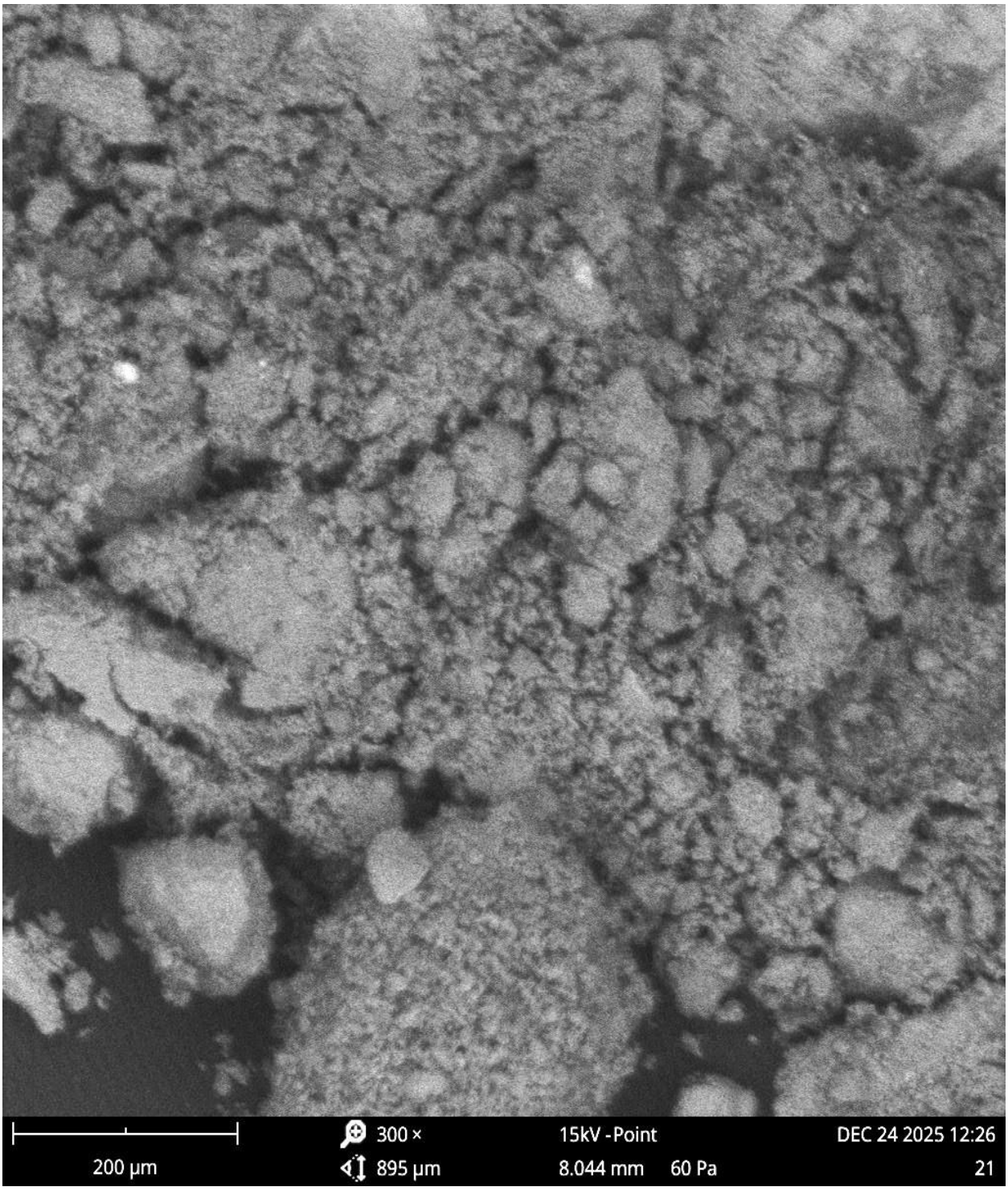

Figure 4.8: Scanning Electron Microscope (SEM) analysis of CaO nanoparticles

Sample ID:Copper Oxide NPs
Sample Scans:32
Background Scans:16
Resolution:4
System Status:Good
Method Name:Transmittance
User:Admin
Date/Time:2025-11-01T19:48:50.291-07:00
Range:4000 - 650
Apodization:Happ-Genzel
File Location:C:\Program Files\Agilent\MicroLab PC\Results\Copper Oxide NPs_11-1-2025T7-48-50 PM.a2r

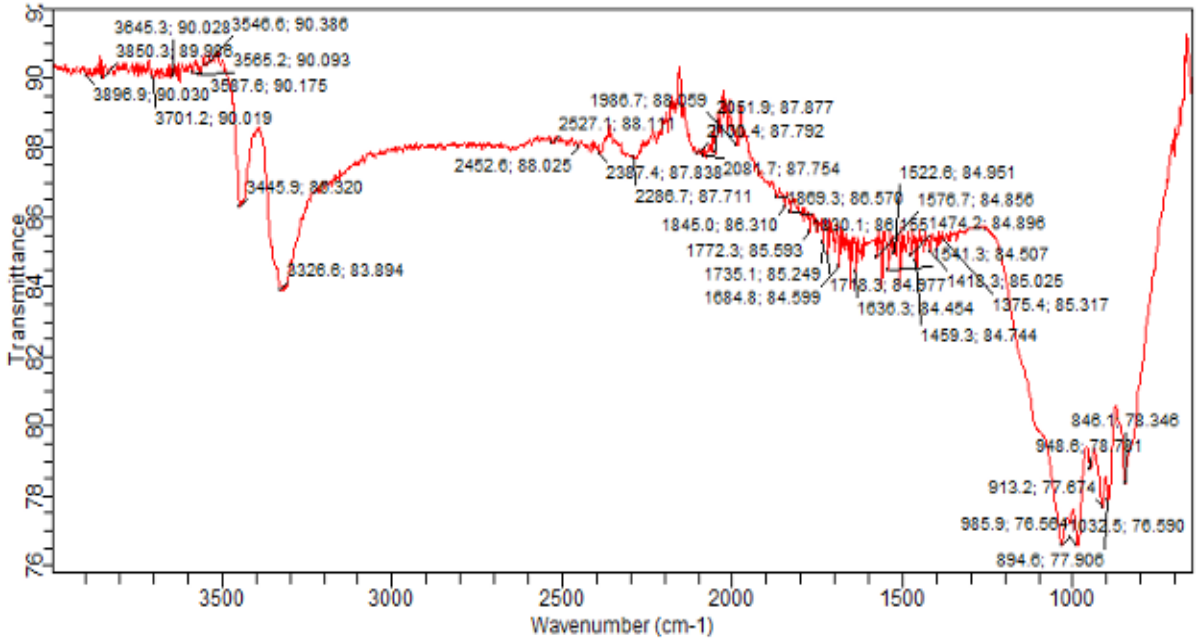

Figure 4.9: Fourier Transform Infrared Spectroscopy analysis for CuO nanoparticle

Sample ID:Copper Oxide + Calcium Oxide NPs
Method Name:Transmittance
Sample Scans:32
User:Admin
Background Scans:16
Date/Time:2025-11-01T19:45:57.622-07:00
Resolution:4
Range:4000 - 650
System Status:Good
Apodization:Happ-Genzel
File Location:C:\Program Files\Agilent\MicroLab PC\Results\Copper Oxide + Calcium Oxide NPs_11-1-2025T7-45-57 PM.a2r

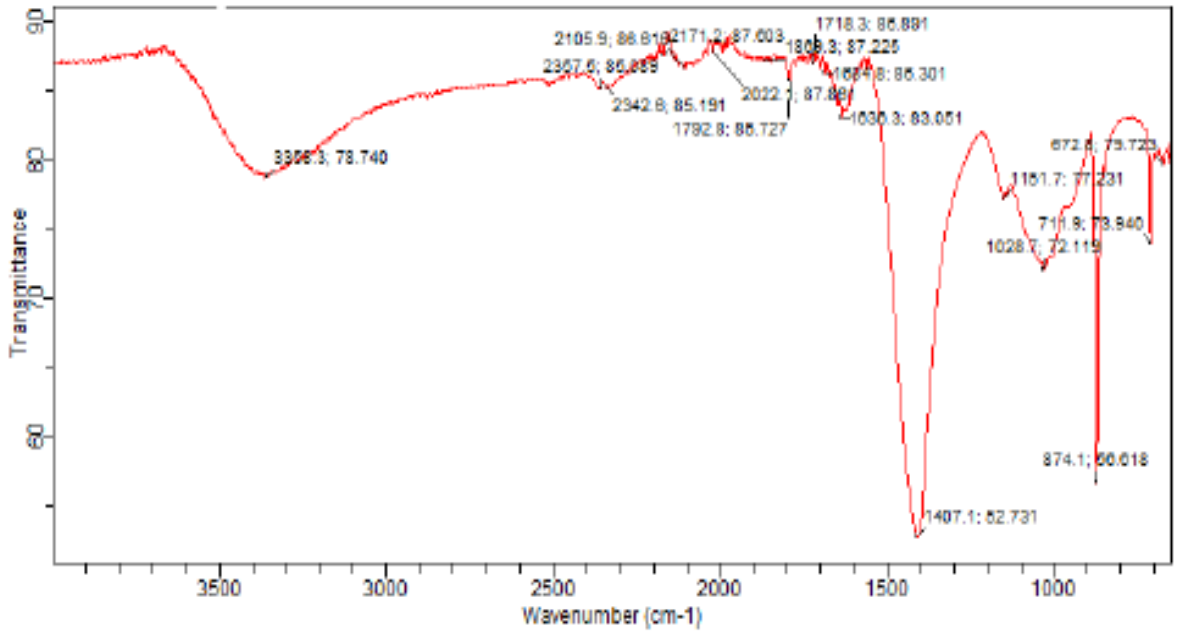

Figure 4.10: Fourier Transform Infrared Spectroscopy analysis for CaO- CuO binary nanoparticle

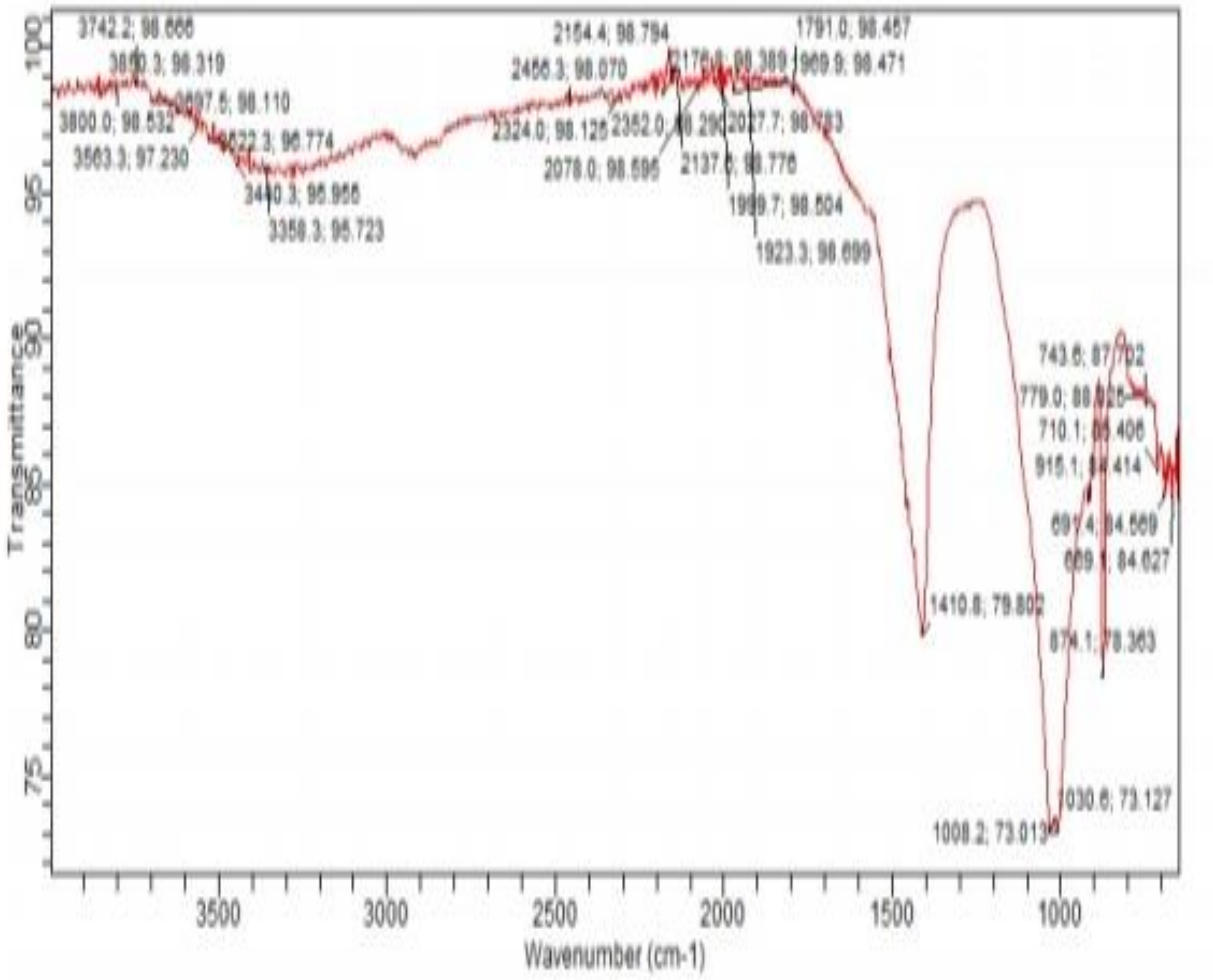

Figure 4.11: Fourier Transform Infrared Spectroscopy analysis for CaO- CuO binary nanoparticle

Table 4.5: Result of the effect of catalyst (CuO) dose on photocatalytic degradation of petroleum wastewater.

Catalyst dose	COD treated (CuO)	%COD Reduction (CuO)	COD treated (CaO)	%COD Reduction (CaO)	COD Treated (CaO-CuO)	%COD Reduction (CaO-CuO)
0.125	222.32	90.71	218.681	91.472	158.74	93.37
0.100`	411.04	82.83	394.121	84.630	265.16	88.92
0.075	521.37	78.22	528.106	79.403	401.05	83.24
0.050	608.11	74.59	589.160	77.023	559.74	76.61
0.025	778.12	67.49	770.549	69.951	681.97	71.51

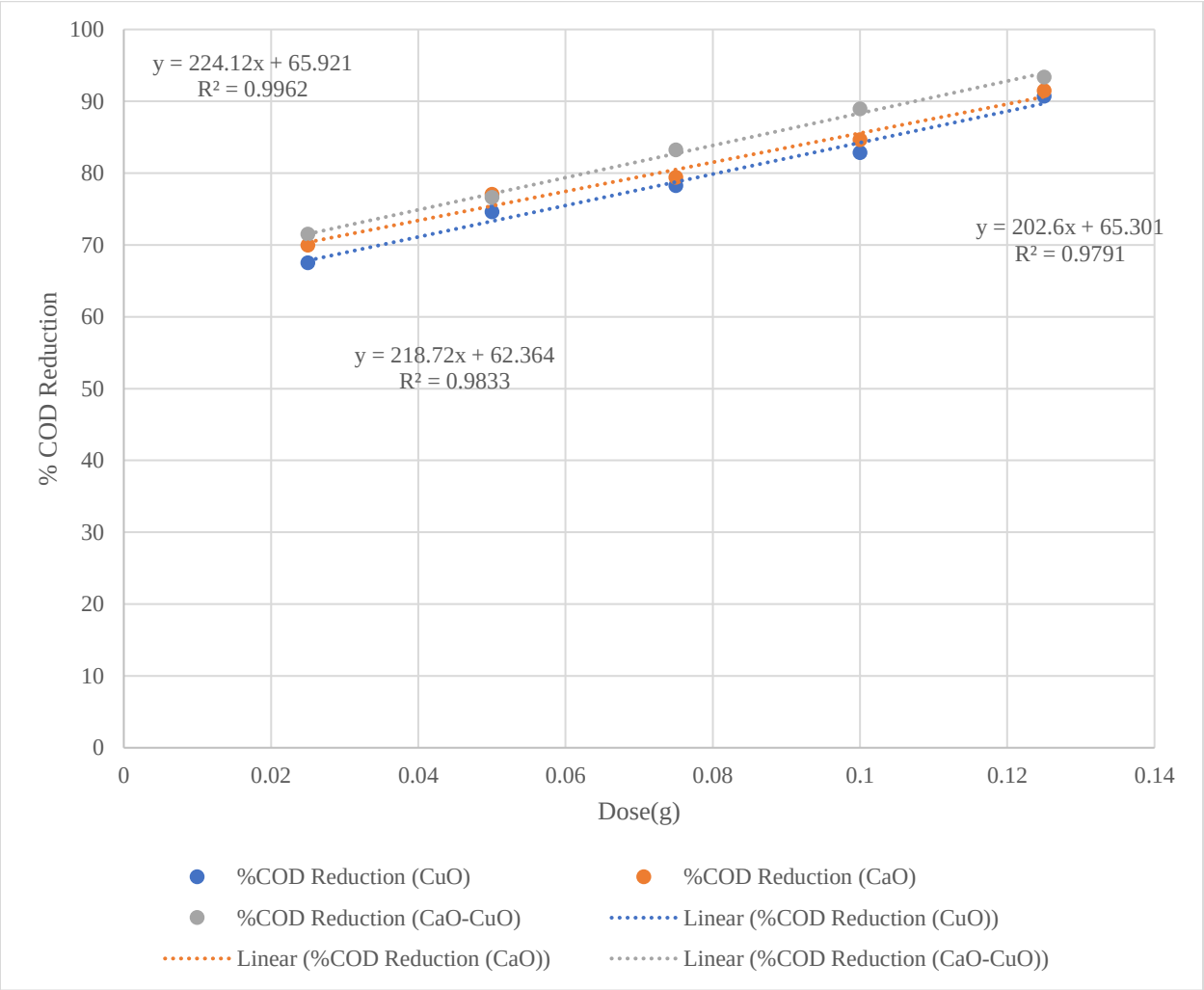

Figure 4.12: A graph of the effect of catalyst dose on photocatalytic degradation of petroleum wastewater.

Table 4.6: Result of the effect of pH on photocatalytic degradation of petroleum wastewater.

pH	COD treated (CuO)	%COD Reduction (CuO)	COD treated (CaO)	%COD Reduction (CaO)	COD Treated (CaO-CuO)	%COD Reduction (CaO-CuO)
2	247.34	89.67	254.772	90.064	163.41	93.17
4	209.22	91.26	261.847	89.788	101.23	95.77
6	265.94	88.89	273.016	89.353	164.61	93.12
8	302.59	87.36	298.554	88.357	172.19	92.81
10	341.72	85.72	339.599	86.756	206.28	91.38

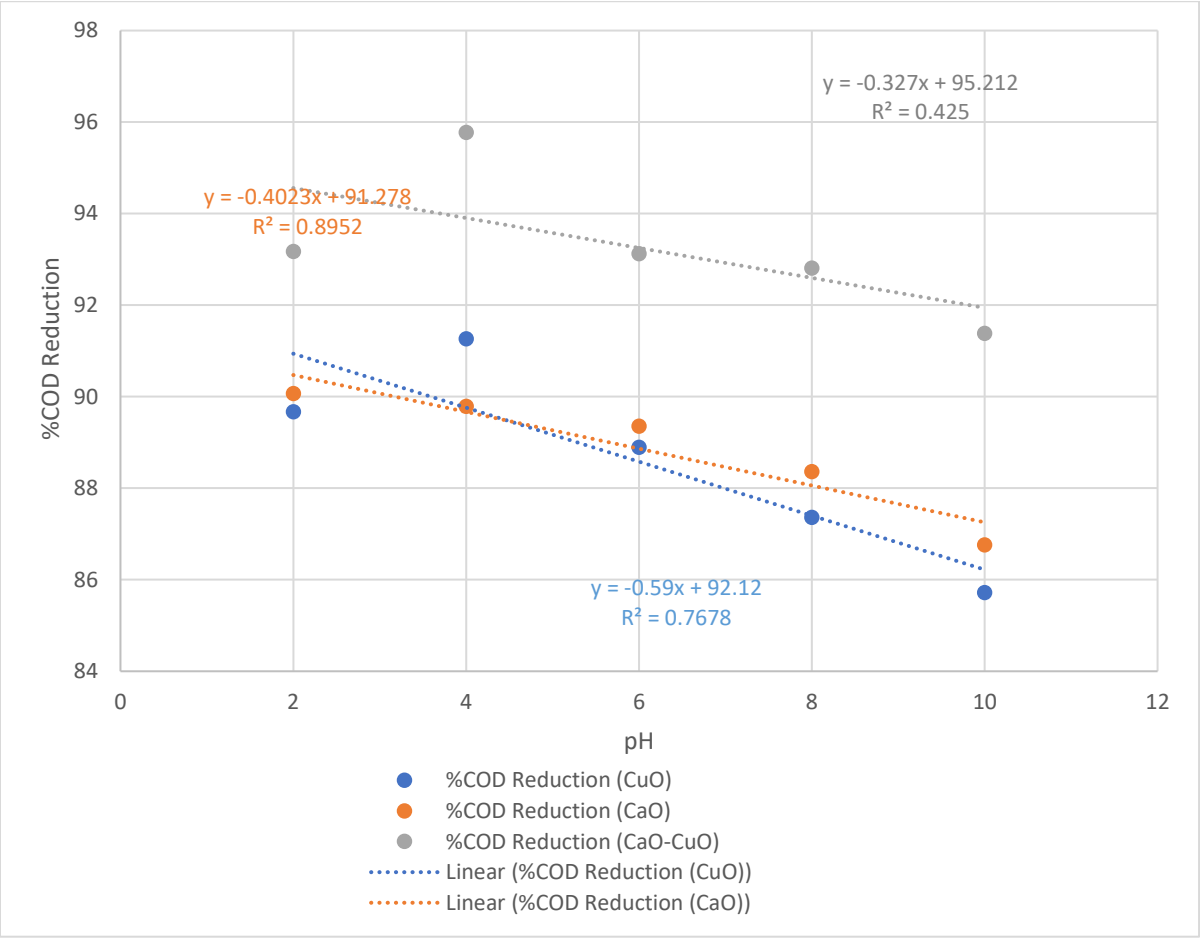

Figure 4.13: A graph of the effect of pH on photocatalytic degradation of petroleum wastewater.

Table 4.7: Result of the effect of contact time on photocatalytic degradation of petroleum wastewater.

Contact time (mins)	COD treated (CuO)	%COD Reduction (CuO)	COD treated (CaO)	%COD Reduction (CaO)	COD Treated (CaO-CuO)	%COD Reduction (CaO-CuO)
30	2036.12	14.93	2020.97	21.19	1849.60	22.73
60	1897.23	20.74	1882.03	26.37	1507.41	37.02
90	1549.71	35.26	1529.42	40.36	1188.32	50.35
120	1140.51	52.35	1157.39	54.87	809.02	66.20
150	796.20	66.74	805.30	68.60	550.13	77.02
180	524.83	78.07	509.56	80.13	383.75	83.97
210	364.23	84.78	355.68	86.13	234.14	90.22
240	301.45	87.41	292.80	88.58	162.14	93.23
270	253.34	89.42	250.73	90.22	112.30	95.31
300	212.87	91.11	206.59	91.94	101.59	95.76

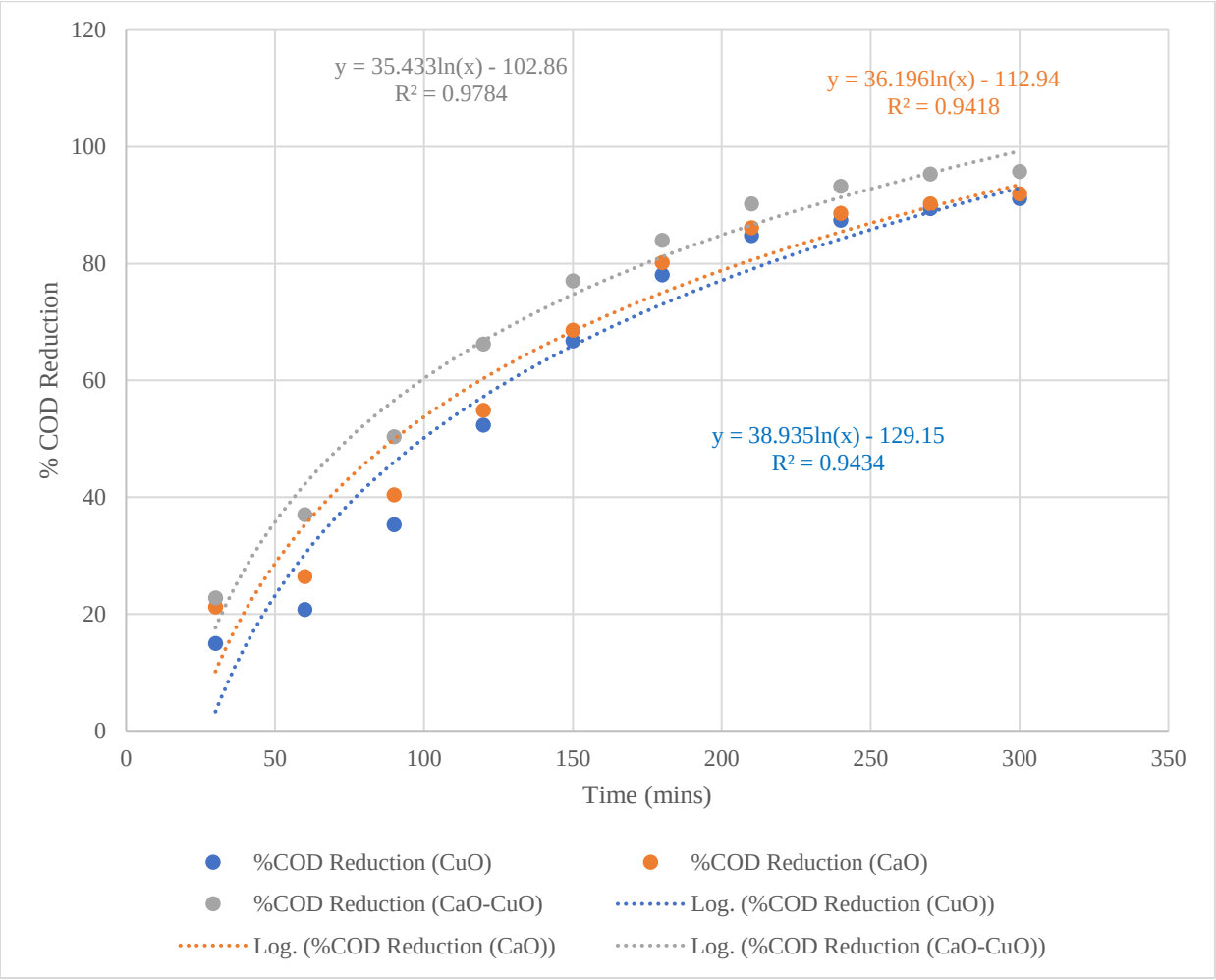

Figure 4.14: A graph of the effect of contact time on photocatalytic degradation of petroleum wastewater.

Table 4.8: A table showing the comparative analysis of Physicochemical properties of the untreated petroleum wastewater(PEWW), petroleum wastewater treated with CuO nanoparticles (CuOTPEWW), and petroleum wastewater treated with CaO-CuO nanoparticles (BTPEWW).

S/N	PARAMETERS	PEWW	CuOTPEWW	CaOTPEWW	BTPEWW
1	pH	8.37±0.02	6.80±0.0	7.02±0.0	6.27±0.36
2	Electrical conductivity (µs/cm)	645.67±2.33	267±0.47	273.67±1.45	267±0.47
3	Total Dissolved Solids (mg/L)	355.12±1.28	157.85±0.95	150.52±0.80	146.85±0.32
4	Temperature (^{o}C)	24.43±0.03	35.00±0.00	32.00±0.00	35.07±0.04
5	Total Suspended Solids (mg/L)	2.40±0.12	ND	ND	ND
6	Total Solids (mg/L)	357.52±1.25	157.85±0.95	150.52±0.80	146.85±0.32
7	Chloride (mg/L)	242.31±2.09	242.31±2.09	216.35±6.63	242.31±2.09
8	Dissolved Oxygen (mg/L)	3.30±0.06	6.03±0.03	6.03±0.03	5.30±0.17
9	Biological Oxygen Demand(mg/L)	17.20±0.30	8.07±0.09	8.07±0.09	6.70±0.36
10	Chemical Oxygen Demand (mg/L)	2393.56±85.59	206.85±2.20	191.28±0.96	109.75±1.63
11	Phosphate (mg/L)	19.32±0.46	21.38±1.08	21.38±1.08	10.11±0.19
12	Sulphate (mg/L)	27.45±0.28	24.15±0.40	24.15±0.40	25.02±1.13
13	Nitrate (mg/L)	89.53±1.20	50.03±3.54	50.03±3.54	60.84±1.82
14	Total Hydrocarbon (mg/L)	1357.15±18.28	26.01±1.29	30.71±0.19	14.94±0.58
15	Turbidity (NTU)	796.64±0.53	63.91±0.19	66.17±2.94	53.37±1.83
16	Total Organic Carbon (%)	796.74±0.53	3.47±0.27	4.00±0.12	1.27±0.19
17	Cadmium (mg/L)	0.09±0.01	BDL	BDL	BDL
18	Lead (mg/L)	0.13±0.03	BDL	BDL	BDL

19	Nickel (mg/L)	0.31±0.003	BDL	BDL	0.11±0.01
20	Copper(mg/L)	0/52±0.01	0.35±0.02	0.30±0.00	0.30±0.01
21	Iron (mg/L)	10.03±0.03	2.13±0.03	2.57±0.13	2.99±0.12

KEY

PEWW = Untreated petroleum wastewater

CuOTPEWW = CuO nanoparticles treated petroleum wastewater

BTPEWW = Binary oxide (CaO – CuO) nanoparticles treated petroleum wastewater

CHAPTER FIVE

DISCUSSION, CONCLUSION AND RECOMMENDATION

5.1: DISCUSSION

This chapter is divided into five, viz. Discussion, Findings, Contribution to knowledge, Conclusion, and Recommendation.

5.1.1: PHYTOCHEMICAL SCREENING OF THE ONION EXTRACT

Table 4.1 shows the phytochemical composition of the aqueous extract of the onion peel. From the result, the onion peel is rich in phytochemicals such as Phenolic, flavonoids, tannins, saponins, terpenoids, and steroids. This is in line with what was reported by Usman *et al*. (2022), and Gorrepati *et al*. (2024). The bioactive compounds present in this extracts, primarily flavonoids and polyphenols, are instrumental in reducing metal ions and mitigating particle agglomeration by capping them (Badawy *et al*., 2021). Additionally, their presence in the extracts enhance the antimicrobial efficacy of the nanoparticles (Kalaiyan *et al*., 2021).

5.1.2: PHYSICOCHEMICAL CHARACTERIZATION OF UNTREATED AND TREATED PETROLEUM WASTEWATER SAMPLES

Table 4.10 presents a comparative analysis of untreated petroleum wastewater (PEWW) against its treated variants utilizing CuO nanoparticles (CuOTPEWW), CaO nanoparticles (CaOTPEWW) and a combination of CaO-CuO nanoparticles (BTPEWW). The results indicate significant enhancements across various parameters post-treatment, particularly concerning the reduction of organic pollutants and heavy metals. The CuO and CaO nanoparticles are individually effective in diminishing contaminants through mechanisms of adsorption and catalytic degradation, while the synergistic effects of the binary CaO-CuO system further amplify treatment efficiency. Untreated

PEWW is characterized by significant pollution levels that are representative of petroleum wastewater, with chemical oxygen demand (COD) and hydrocarbon concentrations that exceed safe discharge thresholds (Ighalo *et al*., 2021).

5.1.2.1: KEY IMPROVEMENTS INDUCED BY TREATMENT

pH Levels: The pH of PEWW was reduced from an alkaline level of 8.37 to near-neutral values of 7.02 ± 0.00 (CaOTPEWW), 6.80 (CuOTPEWW) and 6.27 (BTPEWW), thus aligning with typical water quality standards (6.5-8.5) and facilitating the precipitation of metals (Peng *et al*., 2017).

Electrical Conductivity and Solids: Electrical conductivity decreased from 645.67 µS/cm in PEWW to 267 µS/cm following treatment, suggesting a significant removal of ionic species; total suspended solids (TSS) were ultimately non-detectable (ND) in BTPEWW (Peng *et al*., 2017).

Oxygen Demand and Organic Material: Biochemical oxygen demand (BOD) declined from 17.20 to 6.70 mg/L, while COD decreased from 2393.56 to 109.75 mg/L (a reduction of 95%). Total hydrocarbons were reduced from 1357.15 to 14.94 mg/L (99% reduction), and total organic carbon (TOC) dropped from 9.74% to 1.27% in BTPEWW, underscoring effective photocatalytic and adsorptive degradation processes (Geb *et al*., 2021).

Nutrient Levels: Nitrate concentrations fell from 89.53 to 60.84 mg/L, and phosphate levels decreased from 19.32 to 10.11 mg/L (Peng *et al*., 2017).

Heavy Metal Concentration: Cadmium (Cd) and lead (Pb) concentrations transitioned from detectable levels to below the detection limit (BDL); nickel (Ni) levels decreased from 0.31 to 0.11 mg/L, while iron (Fe) levels diminished from 10.03 to 2.99 mg/L, primarily through adsorption onto the nanoparticles (Peng *et al*., 2017).

A remarkable reduction in COD was observed, decreasing from 2393.56 ± 85.59 mg/L to 206.85 ± 2.20 mg/L**,** 191.28 ± 0.96 mg/L, and 109.75 ± 1.63 mg/L after treatment. The corresponding removal efficiencies were:

- CuOTPEWW: 91.36%
- CaOTPEWW: 92.01%
- BTPEWW: 95.42%

The substantial reduction in COD indicates efficient degradation and adsorption of oxidizable organic pollutants. The superior performance of the binary oxide nanoparticles may be attributed to synergistic catalytic effects and enhanced surface adsorption sites.

Additional Observations: Dissolved oxygen (DO) increased from 3.30 to 5.30 mg/L, thereby promoting improved aerobic conditions; however, turbidity experienced a rise from 9.74 to 53.37 NTU, potentially attributable to residual particulate matter (Peng *et al*., 2017).

5.1.2.2: EFFICACY OF TREATMENT AND MECHANISMS INVOLVED:

BTPEWW demonstrates superior performance compared to CaOTPEWW and CuOTPEWW in reducing COD, THC, TOC, and phosphate levels, suggesting that CaO enhances the catalytic activity and stability of CuO when applied in a binary system. CuO nanoparticles are particularly proficient in the adsorption of heavy metals and organics, achieving over 90% reduction in hydrocarbons. The shifts in pH observed during the treatment process facilitate agglomeration and sedimentation of particles. Furthermore, the elevated temperature (~35°C) following treatment likely contributes to enhanced reaction kinetics. Despite these improvements, residual turbidity,

nitrate, and heavy metal concentrations indicate the necessity for additional polishing steps, such as filtration, to achieve optimal water quality (Ighalo *et al*., 2021).

5.1.3: DYNAMIC LIGHT SCATTERING

The hydrodynamic particle size analysis of CuO nanoparticles revealed a Z-Average of 45.82 nm, which is an important metric that reflects the central tendency of particle sizes in the distribution (Figure 4.1). A low polydispersity index of 0.193 pointed out that the size distribution was fairly narrow and uniform. Apart from a primary peak at 23.74 nm, which occupied nearly 80% of the total intensity, representing the majority of well-dispersed nanoparticles, the rest of the particles displayed secondary peaks at 279.7 nm and around 5154 nm, corresponding to minor agglomerates and sometimes large clusters, demonstrating the presence of larger particle fractions, just like those trends reported in earlier studies by Eid *et al*. (2023). In contrast to the mixed CuO–CaO nanoparticles, which gave a Z-Average much lower at 20.63 nm, though a higher polydispersity index of 0.405 reflects greater variability in particle sizes (Figure 4.2). Its main peak at 15.68 nm characterizes the main population of nanoparticles and a secondary peak at 224 nm that represents mid-sized aggregates, reflecting the effect of different aggregation behaviours for CuO and CaO. As reported by Nzilu, *et al*. (2023), the sizes of CuO nanoparticles detected here fall within the green-synthesized CuO size range of 15–30 nm and have similar heterogeneity patterns. The occurrence of multiple peaks indicates diverse particle sizes in the sample, which is more critical for applications based on controlled nanostructure features. Generally, the CuO nanoparticles demonstrate better monodispersity and dispersion, while the CuO–CaO mixture presented an overall moderate aggregation with higher polydispersity, which agrees with the previous literature (Raja *et al*., 2008).

5.1.4: X-RAY DIFFRACTION ANALYSIS

The diffractogram presented in Figure 4.3 indicates that the sample designated “Copper Oxide Nanoparticle” is predominantly composed of crystalline CuO (tenorite), with additional weak signals corresponding to various copper and aluminosilicate phases (Ighalo *et al*., 2021). The red X-ray diffraction (XRD) pattern reveals sharp peaks at specific 2θ angles that align with the reference pattern for tenorite (CuO), which is illustrated in blue at the lower portion of the plot. Tenorite represents the monoclinic phase of copper(II) oxide and is the anticipated end product in numerous syntheses of CuO nanoparticles. The alignment of peak positions and their relative intensities further corroborates the identification of tenorite as the principal phase. Moreover, reference lines for clinoatacamite (a basic copper chloride hydroxide) and mullite (an aluminosilicate) are depicted in black and green, respectively, beneath the XRD pattern. The coincidence of some reference lines with weak features in the experimental spectrum suggests the presence of trace secondary phases or residual substrate/support materials; however, the significantly lower intensities of these features compared to those of CuO imply that they are likely minor impurities (Darezereshki and Bakhtiari, 2013). A dominant tenorite phase means the sample should exhibit properties typical of CuO, such as p-type semiconducting behavior and strong catalytic and antimicrobial activity. The presence of minor clinoatacamite or mullite could slightly influence surface chemistry or catalytic performance, especially if these phases are concentrated at the particle surface (Slosarczyk *et al*., 2023).

The diffractogram presented in Figure 4.4 is the XRD pattern of synthesized CuO–CaO nanoparticles, and it exhibits sharp reflections characteristic of monoclinic tenorite, CuO, with prominent peaks around 35–38° (2θ), which are indicative that CuO is the dominant crystalline phase (Figure 2). Such peaks agree with previous XRD analyses of CuO nanoparticles, which often

have diffraction at ~35.5° and ~38.6° corresponding to monoclinic CuO reflections along the (002) and (111) planes, respectively (Gebrie et al., 2025). The weaker reflections in the XRD pattern may be assigned to CaO-related phases. Such behaviour is supported by studies on mixed CaO–CuO systems: for instance, in silane-modified CaO–CuO catalysts, (Pranyoto *et al*., 2022) observed XRD peaks corresponding to CaO, $Ca(OH)_2$, and CuO, indicating partial crystallinity and a multi-phase composition. Furthermore, the CuO reflections in our sample display relatively narrow peak widths, implying small but well-ordered crystallites. Similar observations of CuO crystallite size in the nanoscale regime have been made in other composite oxides: for example, in a polystyrene/CuO–Fe_2O_3 nanocomposite, researchers reported tenorite (CuO) peaks at ~35.4° and ~38.8° (2θ), and estimated crystallite sizes in the tens of nanometres. In addition, within a heterogeneous system in which both CuO and CaO coexist with no significant peak shifts, the two oxides probably form discrete nanocrystalline domains rather than a solid solution. This interpretation is supported by the work of Pranyoto et al. (2022) where no major 2θ shifts were reported between the individual oxides in their mixed-metal-oxide XRD patterns.

5.1.5: SCANNING ELECTRON MICROSCOPE (SEM) ANALYSIS

The SEM image shown in Figure 4.5 shows strongly agglomerated, irregular copper-oxide powder with a wide size distribution of aggregates from a few micrometres up to roughly 50–100 μm, typical of nanoparticle-based CuO systems observed at relatively low magnification (300×) (Alabi *et al*., 2013). The field is filled with quasi-spherical to sub-angular grains that cluster into dense aggregates, a phenomenon commonly observed for CuO nanoparticles produced without strong dispersants, as high surface energy drives agglomeration. Similar SEM micrographs of CuO and CaO powders show “granular” or “sponge-like” agglomerates where primary nanoparticles (tens

of nanometres) fuse into micrometre-scale clusters, consistent with the texture seen here (Badawy *et al*., 2021)

The scale bar of 200 µm at 300× magnification indicates that most bright aggregates are tens of micrometres across, meaning each aggregate likely consists of many smaller nano- or submicrometre crystallites rather than single large crystals (Gontrani *et al*., 2023). The rough, porous-looking surfaces of the aggregates resemble the sponge-like morphology reported for CuO powders, which can provide a high specific surface area beneficial for catalytic, sorption, or antimicrobial applications. Studies on CuO nanoparticles emphasise that aggregation state and surface roughness significantly affect properties such as reactivity, bandgap, and interaction with biological or cementitious matrices, so the morphology seen here is consistent with functional CuO-based nanomaterials rather than well-faceted single crystals (Da Costa and Sharma 2016)

The image Figure 4.6 depicts that the majority of particles are spherical in nature and agglomerate, very typical for green-synthesized nanoparticles due to plant-derived biomolecules acting as natural capping agents. The scale bar indicates 200 µm with a nominal magnification of 300×, so each bright-gray feature is on the order of a few to several tens of micrometers across, representing clusters rather than individual primary nanoparticles. At 15 kV accelerating voltage and BSD (backscattered electron) imaging, contrast mainly reflects average atomic number and local topography, which is consistent with dense oxide grains packed into a rough surface. This observation is in good agreement with reports of biosynthesized metal oxide nanoparticles (Gontrani *et al*., 2023, Amaliyah *et al*., 2020; Mali *et al*., 2019).

5.1.6: ENERGY DISPERSIVE X-RAY SPECTROSCOPY (EDS) ANALYSIS

Tables 4.2 and 4.3 show the elemental composition of CuO nanoparticles and CaO – CuO binary nanoparticles. While Table 4.2 shows that copper is the major component of the synthesized CuO nanoparticles, with a composition of 88.73wt%, Table 4.3 confirms that copper and calcium are the two major components of the synthesized CaO – CuO binary nanoparticles, with 69.12 wt% Cu and 15.67 wt% Ca, respectively, suggesting the successful formation of the CuO and CaO phases within the nanocomposite material. Minor quantities of Cl (3.36, 6.91 wt%), C (1.60, 2.07 wt%), and Si (1.48, 0.98 wt%) were also detected, probably of residual plant phytochemicals or precursor material origin in the synthesis. Trace elements such as Ag, S, Sn, K, Ni, Fe, Al, Cr, and P were present in very small proportions (<1 wt%), which is common in green synthesis due to natural impurities or instrument-related background signals. The low levels of these traces do not affect the overall composition.

5.1.7: THE FOURIER-TRANSFORM INFRARED (FTIR) SPECTROSCOPY ANALYSIS

Figure 4.5 **is t**he FTIR spectrum of the synthesized CuO nanoparticles. It confirms that molecules from the onion peel extract successfully attached to the surface of the copper oxide nanoparticles. The key evidence is the presence of specific chemical fingerprints in the graph. The very broad, strong dip around 3445.9 cm^{-1} is the signature of hydroxyl groups (O-H). These groups, found in natural compounds like phenols from the onion, act as the reducing agents needed to transform the copper precursor into nanoparticles. Additionally, the dips between 1600 and 1750cm^{-1} (e.g., 1772.3cm^{-1}, 1684.8 cm^{-1}) are from the C=O (carbonyl) groups of other organic molecules. These C=O and O-H compounds coat the surface of the nanoparticles like a protective shell, acting as capping or stabilizing agents to prevent them from clumping together (aggregation). In short, the

spectrum proves the "green" nature of the synthesis by showing the plant compounds are integrated with the copper chloride nanoparticles (Amaliyah *et al*., 2020, Pasieczna-Patkowska, *et al*., 2025).

Figure 4.6 illustrates the FTIR spectrum of CuO – CaO binary Nanoparticles. It showed the chemical bonds and surface features of the synthesized material. By focusing on the prominent peaks, which include (3356 cm^{-1}, 1407 cm^{-1}, 1028.7 cm^{-1}, 874.1 cm^{-1}, 711.9 cm^{-1}, 672.8 cm^{-1}), one can gain insight into both the internal structure of the metal oxides and their surface chemistry. A broad peak at 3356 cm^{-1} reflects the O–H stretching vibrations, indicating the presence of surface hydroxyl groups and adsorbed water. This is expected for metal oxide nanoparticles, which often retain moisture due to their high surface area (Nzilu *et al*., 2023). The peak at 1407 cm^{-1} corresponds to carbonate (CO_3^{2-}) stretching, indicating slight surface carbonation of CaO, likely from exposure to atmospheric CO_2. Peaks at 1028.7 cm^{-1} and 874.1 cm^{-1} are characteristic of Ca–O lattice vibrations and stretching, confirming the formation of calcium oxide (Periakaruppan *et al*., 2025). In the lower-frequency region, peaks at 711.9 cm^{-1} and 672.8 cm^{-1} are attributed to Cu–O lattice vibrations and stretching, confirming the successful formation of copper oxide in its tenorite phase (Dehaj and Mohiabadi, 2019).

5.1.8: THE EFFECT OF CONTACT TIME ON PHOTOCATALYTIC DEGRADATION OF PETROLEUM WASTEWATER.

Figure 4.9 is a graph of the effect of contact time as well as the rate of photocatalytic degradation of petroleum wastewater. It illustrates that the removal of chemical oxygen demand (COD) increases with contact time for both CuO nanocatalyst, CaO nanocatalyst, and CaO-CuO binary nanocatalyst, adhering to a logarithmic trend that approaches a plateau near 100% removal. The

x-axis represents the contact or degradation time, ranging from approximately 0 to 300 minutes, while the y-axis indicates the %COD removal, extending from 0 to about 120%.

The catalysts exhibit a rapid increase in %COD removal during the initial phase (0–100 minutes), followed by a more gradual rise. This suggests that the early degradation of readily oxidizable organic matter occurs quickly, whereas the removal of more resistant compounds takes place at a slower rate—an observation frequently documented in the context of COD reduction through advanced oxidation and biological processes (Soares *et al*., 2022).

From the graph, it is observed that the CuO and CaO nanocatalysts have a logarithmic equations of the form $y = 38.935 \ln(x) - 129.15$ and $36.196\ln(x) – 112.94$, respectively, which fits the data, with coefficient of determination $R^2 = 0.9434$ and 0.9418 respectively, indicating reasonably strong yet slightly less precise fit to the experimental data. Conversely, CaO-CuO binary nanocatalyst is represented by the equation $y = 35.433 \ln(x) - 102.86$, which exhibits a higher coefficient of determination $R^2 = 0.9784$. This suggests that the logarithmic model accurately characterizes its kinetics, allowing for more consistent predictions of removal efficiency over time (Sangoremi 2025).

Throughout the majority of the observed time range, the data points for the CaO-CuO nanocatalyst are situated above those for the CuO and CaO nanocatalysts, indicating higher COD removal efficiencies for the corresponding contact times. By about 250–300 minutes, the nanocatalysts approach removal efficiencies of 90–100%. However, the CaO-CuO nanocatalyst achieves significant removal percentages earlier (approximately 80% removal is attained around 150–180 minutes), suggesting faster kinetics and possibly reduced retention times required in treatment reactors.

The logarithmic equation $y = a \ln(x) + b$ aligns with reaction mechanisms governed by rapid initial adsorption or oxidation, followed by slower reactions involving residual organics. This behavior is akin to a pseudo-first-order response, a concept often discussed in the wastewater treatment literature (Nasser *et al*., 2024). The high coefficient of determination, R^2 (exceeding 0.94), indicates that, within the evaluated time range, contact time is the predominant variable influencing COD removal under fixed operating conditions (Imteaz *et al*., 2025). Consequently, the fitted models can be employed for approximate design purposes or to predict the contact time necessary for achieving a specific target COD removal efficiency.

5.2: FINDINGS.

The findings from this study are as follows:

1. Onion peel extract is rich in phytochemicals such as flavonoids, phenolics, tannins, saponins, and Alkaloids.
2. Synthesized calcium oxide nanoparticles were of nano size
3. Synthesized copper oxide nanoparticles were of nano size
4. Synthesized calcium oxide -copper oxide nanoparticles were of nano size.
5. Synthesized nanocatalysts (CuO, CaO and CaO-CuO) are crystalline in nature, spherical and agglomerated, with copper as the major component of CuO and Calcium the major component for CaO. At the same time, CaO-CuO binary has copper and calcium as the major components. The O-H group found in the synthesized nanoparticles indicates the presence of natural compounds such as phenolics from the onion peel extract
6. The petroleum wastewater was highly polluted, above the threshold limit
7. Both nanocatalysts degraded the petroleum wastewater.
8. The degradation reaction for both catalysts is a pseudo-first-order reaction
9. Treatment greatly improves the physicochemical properties of the wastewater.

5.3: CONTRIBUTION TO KNOWLEDGE

This study has contributed to knowledge in the following ways:

1. CuO, CaO and CaO-CuO nanocatalysts were successfully synthesized using onion peel extract.
2. Revealed the nanocatalysts successfully degraded petroleum contaminants in petroleum wastewater
3. Established that the degradation process follows a pseudo-first-order reaction.

5.4: CONCLUSION

This Research focused on the green synthesis and characterization of copper oxide nanoparticles and calcium oxide-copper oxide binary nanoparticles using onion peel extract as precursor material, as well as comparing their photocatalytic abilities in the degradation of petroleum-contaminated wastewater. In the course of this study, the onion peel samples were extracted using the decoction method, and the extract was used in the synthesis of the metal oxide nanoparticles. These synthesized nanoparticles were characterized and subjected to photocatalytic degradation of petroleum-contaminated wastewater. It was observed from the study that calcium oxide–copper oxide binary nanoparticles have better characteristic properties as well as photocatalytic degradation ability than copper oxide nanoparticles. This is attributed to the synergistic effect between Calcium oxide and Copper oxide, which enhances the separation of charge carriers and increases the surface area. The green synthesis approach used in this study offers a cost-effective and eco-friendly method for the production of metal oxide nanoparticles for environmental applications.

5.5: RECOMMENDATION

Subsequent research should look at this photocatalytic degradation study under a controlled system using UV light irradiation and apply a design expert, such as Response Surface Methodology, in optimization of the synthesis and degradation process.

REFERENCES

Abdel-Shafy, H. I. and Mansour, M. S. (2016). A review on polycyclic aromatic hydrocarbons: source, environmental impact, effect on human health, and remediation. Egyptian Journal of Petroleum 25(1): 107-123.

Ademoroti, C.M.A. (1996). Standard Methods for Water and Effluent Analysis. Foludex Press Ltd., Ibadan 20 -150.

Adofo Y. k., Nyankson E., and Agyei-Tuffour B. (2022). Dispersants as an oil spill clean-up technique in the marine environment: A review. Heliyon 8(8): 1-19

Ahmed, S. N. and Haider, W. (2018). Heterogeneous photocatalysis and its potential applications in water and wastewater treatment: A review. Nanotechnology 29(34): 1-30

Ahmed, S., Saeed, M. and Iqbal, S. (2018). Eco-friendly synthesis of copper oxide nanoparticles using citrus lemon peel extract and their antibacterial activity. Journal of Cleaner Production 170: 879-887.

Aklilu G. B., Lemma T. T., Osman A. Z., Mahendra G., Jaebeom L., and Fedlu K. S. (2022). Green Synthesis of a CuO–ZnO Nanocomposite for Efficient Photodegradation of Methylene Blue and Reduction of 4-Nitrophenol. ACS Omega 7 (35): 30908-30919

Alabi, A. B. Coppede, N. Vilani, M. Calestani, D. Zappetini, A. Babalola, O. A. and Salvatore, I. (2013). Photocatalytic activity of nanostructured copper (ii) oxide particles. Ife Journal of Science 15(2): 409-414

Altammar, K. A. (2023). A review on nanoparticles: Characteristics, synthesis, applications, and challenges. Frontiers in Microbiology 14: 1-24.

Amaliyah, S., Pangesti, D. P., Masruri, M., Sabarudin, A. and Sumitro, S. B. (2020). Green synthesis and characterization of copper nanoparticles using Piper retrofractum Vahl extract as bioreductor and capping agent. Heliyon 6(8): 1-20

Ansari, S. A. Khan, M. M., Ansari, M. O. and Cho, M. H. (2016). "Biogenic synthesis, photocatalytic, and photoelectrochemical performance of Ag-ZnO nanocomposite," Journal of Physical Chemistry C 117(51): 27023-27030.

Badawy, A. A., H Abdelfattah, N. A., Salem, S. S., Awad, M. F. and Fouda, A. (2021). Efficacy Assessment of Biosynthesized Copper Oxide Nanoparticles (CuO-NPs) on Stored Grain Insects and Their Impacts on Morphological and Physiological Traits of Wheat (Triticum aestivum L.) Plant. Biology 10(3): 233-246

Chakraborty, N., Banerjee, J., Chakraborty, P., Banerjee, A., Chanda, S., Ray, K., Sarkar, J. (2022). Green synthesis of copper/copper oxide nanoparticles and their applications: a review. Green Chemistry Letters and Reviews 15(1): 187–215.

Chen, J., Jiang, Y., Liu, X., Xia, W., Huang, A., Zong, J., Wang, Z., Qian, B. and Donat, F. (2024). One-step synthesis of CaO/CuO composite pellets for enhanced CO_2 capture performance in a combined Ca/Cu looping process via a facile gel-casting technique. Separation and Purification Technology 328: 125-157.

Da Costa M.V.J. and Sharma P.K. (2016). Effect of copper oxide nanoparticles on growth, morphology, photosynthesis, and antioxidant response in Oryza sativa. Photosynthetica 54 (1): 110-119.

Darezereshki E. and Bakhtiari F. (2013). Synthesis and characterisation of tenorite (CuO) nanoparticles from smelting furnace dust (SFD). Journal of Mining and Metallurgy Section B Metallurgy 49(1):21-26

Dehaj, M. S. and Mohiabadi, M. Z. (2019). Experimental study of water-based CuO nanofluid flow in heat pipe solar collector. Journal of Thermal Analysis and Calorimetry, 137(6): 2061–2072.

Dhaka, A., Chand Mali, S., Sharma, S., and Trivedi, R. (2023). A review on biological synthesis of silver nanoparticles and their potential applications. Results in Chemistry, 6, 101108.

Elattar, M. M., Darwish, R. S., Hammoda, H. M., and Dawood, H. M. (2024). An ethnopharmacological, phytochemical, and pharmacological overview of onion (Allium cepa L.). Journal of Ethnopharmacology 324: 117-137.

Fujishima, A., Zhang, X. and Tryk, D. A. (2008). TiO_2 photocatalysis and related surface phenomena. Surface Science Reports 63(12): 515-582.

Gaya, U. I., and Abdullah, A. H. (2008). Heterogeneous photocatalytic degradation of organic contaminants over titanium dioxide: A review of fundamentals, progress, and problems. Journal of Photochemistry and Photobiology C: Photochemistry Reviews 9(1), 1-12.

Gontrani, L., Bauer, E. M., Talone, A., Missori, M., Imperatori, P., Tagliatesta, P. and Carbone, M. (2023). CuO Nanoparticles and Microaggregates: An Experimental and Computational Study of Structure and Electronic Properties. Materials 16(13): 1-27.

Gorrepati, K., Kumar, A., Ahammed S. T. P., Khan, Z., Satpute, P., Anandhan, S., Arunachalam, T., Yalamalle, V. R., Mahajan, V. and Singh, M. (2024). Characterization and evaluation of antioxidant potential of onion peel extract of eight differentially pigmented short-day onion (Allium cepa L.) varieties. Frontiers in Sustainable Food Systems 8: 1- 30.

Gunawan, D., Zhang, J., Li, Q., Toe, C. Y., Scott, J., Antonietti, M., Guo, J., and Amal, R. (2024). Materials Advances in Photocatalytic Solar Hydrogen Production: Integrating Systems and Economics for a Sustainable Future. Advanced Materials 36(42): 1- 22.

Haider, F. U., Zulfiqar, U., Ul Ain, N., Hussain, S., Maqsood, M. F., Ejaz, M., Yong, J. W. H. and Li, Y. (2024). Harnessing plant extracts for eco-friendly synthesis of iron nanoparticle (Fe-NPs): Characterization and their potential applications for ameliorating environmental pollutants. Ecotoxicology and Environmental Safety 28: 564 - 593

Hanna, D. H., Nady, D. S., Wasef, M. W., Fakhry, M. H., Mohamed, F. S., Isaac, D. M., Kirolos, M. M., Azmy, M. S., Hakeem, G. E. and Fathy, C. A. (2025). Plant-derived nanoparticles: Green synthesis, factors, and bioactivities. Next Materials 9: 101-127.

Hemmami, H., Zeghoud, S., Ben Amor, I., Alnazza Alhamad, A., Tliba, A., Alsalme, A., Cornu, D., Bechelany, M. and Barhoum, A. (2024). Green synthesis of CaO nanoparticles from chicken eggshells: Antibacterial, antifungal, and heavy metal (Pb^{2+}, Cr^{2+}, Cd^{2+} and Hg^{2+}) adsorption properties. Frontiers in Environmental Science 12: 245-285.

Ighalo, J. O., Sagboye, P. A., Umenweke, G., Ajala, O. J., Omoarukhe, F. O., Adeyanju, C. A., Ogunniyi, S. and Adeniyi, A. G. (2021). CuO nanoparticles (CuO NPs) for water treatment: A review of recent advances. Environmental Nanotechnology, Monitoring and Management 15: 1-18.

Imteaz A. M., Tariq R. M., Rajabi Z. and Ahsan A. (2025). Mathematical Modelling for Predicting Wastewater Treatment Efficiency Through Specialised Electrocoagulation. International Journal of Environmental Research and Education 19(118): 1-28

Iravani, S. (2011). Green synthesis of metal nanoparticles using plants. Green Chemistry 13(10), 2638-2650

Kalaiyan G., Suresh S., Prabu K.M., Thambidurai S., Kandasamy M., Pugazhenthiran N., Kumar S. K., and Muneeswaran T. (2021). Bactericidal activity of Moringa oleifera leaf extract assisted green synthesis of hierarchical copper oxide microspheres against pathogenic bacterial strains. Journal of Environmental Chemical Engineering 9(1). 104847,

Karthik P., Ravichandran S., Sasikala V., Prakash N., Mukkannan A. and Rajesh J. (2023). Effective photodegradation of organic water pollutants by the facile synthesis of Ag_2O nanoparticles. Surfaces and Interfaces 40: 1-18.

Khan S., Noor A., Khan I., Mohammad M., Sadiq M. and Mohammad N. (2023). Photocatalytic degradation of organic dyes contaminated aqueous solution using binary $CdTiO_2$ and ternary $NiCdTiO_2$ nanocomposite. Catalysis 13(1):44

Khan M., Afzal M. and Siddiq M. (2020). Green nanotechnology: sustainable synthesis of metal nanoparticles using plant extracts. Environmental Chemistry Letter, 18: 211-230.

Kharissova O. V. Rasika Dias H. V., Kharisov B. I., Pérez B. O. and Pérez V. M. J. (2013). The greener synthesis of nanoparticles. Trends in Biotechnology 31(4): 240-248.

Kumar S., Singla S. and Shukla A. (2019). Eco-friendly synthesis of calcium oxide nanoparticles using Azadirachta indica leaf extract. Materials Today: Proceedings 20: 365-370.

Lim, M. W., Lau, E. V., and Poh, P. E. (2016). A comprehensive guide of remediation technologies for oil-contaminated soil; Present works and future directions. Marine Pollution Bulletin, 109(1), 14 – 45.

Low J., Yu J., Jaroniec M., Wageh S. and Al-Ghamdi A. A. (2017). Heterojunction photocatalysts. Advanced Materials 29(20): 1-32.

Ly P., Ly K., Phan H., Nguyen H. H., Duong V. and Nguyen H. V. (2024). Recent advances in surface decoration of nanoparticles in drug delivery. Frontiers in Nanotechnology 6:1456-1479.

Mahrsi, M. I., Chouchene, B., Gries, T., Carre, V., Medjahdi, G., Ayari, F., Balan, L., and Schneider, R. (2024). 0D/1D CuO-Cu_2O/ZnO p-n heterojunction with high photocatalytic activity for the degradation of dyes and Naproxen. Journal of Environmental Chemical Engineering 12(3): 136-157.

Mali, S. C., Raj, S., and Trivedi, R. (2019). Biosynthesis of copper oxide nanoparticles using Enicostemma axillare (Lam.) leaf extract. Biochemistry and Biophysics Reports 20: 1-18

Marlina E., Goh S., Wu T., Tan T., Abd H., Sharifah B., and Joan J. C. (2015). Evaluation on the photocatalytic degradation activity of reactive blue 4 using pure anatase nano –TiO_2. Sains Malaysians. 44: 10 - 19

Mittal, A. K., Chisti, Y. and Banerjee, U. C. (2013). Synthesis of metallic nanoparticles using plant extracts. Biotechnology Advances 31(2): 346-356.

Moodi, Z., Bagherzade, G., and Peters, J. (2021). Quercetin as a Precursor for the Synthesis of Novel Nanoscale Cu (II) Complex as a Catalyst for Alcohol Oxidation with High Antibacterial Activity. Bioinorganic Chemistry and Applications 2021: 1-9.

Naseem, T. and Durrani, T. (2021). The role of some important metal oxide nanoparticles for wastewater and antibacterial applications: A review. Environmental Chemistry and Ecotoxicology 3: 59-75.

Nasir, G., Batool, F., Noreen, S., Gondal, H. Y., Mustaqeem, M., Saeed, Z., Gul, Y., Ur Rehman, F. and Ali, H. M. (2024). Biosynthesis of calcium oxide nanoparticles by employing Mulberry (Morus nigra) leaf extract as an efficient source for Rhodamine B remediation. Scientific Reports 14(1): 237- 264.

Nasser Mohamed Sahmoune, Abbas Moussa, and Trari Mohamed (2024). Understanding the rate-limiting step adsorption kinetics onto biomaterials for mechanism adsorption control. Progress in Reaction Kinetics and Mechanism 49: 1–26

Nzilu, D. M., Madivoli, E. S., Makhanu, D. S., Wanakai, S. I., Kiprono, G. K. and Kareru, P. G. (2023). Green synthesis of copper oxide nanoparticles and its efficiency in degradation of rifampicin antibiotic. Scientific Reports 13: 240-270.

Oghenefejiro O. P., Ikhuoria E. U., Ehigie A. C., Osarobo J. A. and Ifijen, I. H. (2025). Green Synthesis of Calcium Oxide Nanoparticles Using Mango (Mangifera indica) Leaf Extract: A Sustainable Approach for Enhanced Antimicrobial Applications.Biomedical Materials and Devices, 3: 1124 – 1144

Ossai, I. C., Ahmed, A., Hassan, A. and Hamid, F. S. (2020). Remediation of soil and water contaminated with petroleum hydrocarbons: A review. Environmental Technology and Innovation, 17: 896-941.

Otabor, G. O., Ikhuoria, E. U., Onaifo, J. O., Ifijen, I. H., Ehigie, A. C. and Aigbodion, A. I. (2025). Comparative Thermogravimetric and Differential Thermal Analysis of Bio-synthesised MgO-Nanoparticles using Chromolaena odorata, Hevea brasiliensis, and Elaeis guineensis Leaf Extracts. Tropical Journal of Chemistry 1(1): 1-7.

Padil Thekkae VV. and Cernik M. (2013) Green synthesis of copper oxide nanoparticles using gum karaya as a biotemplate and their antibacterial application. International Journal of Nanomedicine.8: 889-98.

Pasieczna-Patkowska, S., Cichy, M. and Flieger, J. (2025). Application of Fourier transform infrared (FTIR) spectroscopy in characterization of green synthesized nanoparticles. Molecules 30(3): 684-713.

Periakaruppan, R., Anandhan, L., Palanimuthu, V., Kathiravan, N., Selvaraj, K. S. V. and Al-Dayan, N. (2025). Biogenic synthesis and characterization of calcium oxide nanoparticles using bark extract of Syzygium cumini and an evaluation of their cytotoxicity and wound healing properties. Applied Biochemistry and Biotechnology 197(10): 6592–6603.

Pranyoto, N., Dewi Susanti, Y., Joseph Ondang, I., Angkawijaya, A. E., Edi Soetaredjo, F., Santoso, S. P., Yuliana, M., Ismadji, S. and Hartono, S. B. (2022). Facile synthesis of silane-modified mixed metal oxide as catalyst in transesterification processes. Nanomaterials 12(2): 245-278.

Prathamesh R. S., Kajal S. J., Pooja R. H., Ravindra L. B., Samiksha D. M, and Atharv V. K., (2024). Nanoparticles: Classification, types and applications: A comprehensive review. GSC Biological and Pharmaceutical Sciences 29(03): 190-197

Puiso, J., Paskevicius, A., Zvirgzdas, J., Dimitrova, T. L., Litvakas, A. and Adliene, D. (2023). Application of Red Onion Peel Extract for Green Synthesis of Silver Nanoparticles in Hydrogels Exhibiting Antimicrobial Properties. Gels 9(6): 498-524.

Raha, S. and Ahmaruzzaman, M. (2022). A novel Ag/g-C_3N_4/ZnO/Fe_3O_4 nanohybrid superparamagnetic photocatalyst for efficient degradation of emerging pharmaceutical contaminant (Pantoprazole) from aqueous sources. Journal of Environmental Chemical Engineering, 10(6):1345-1378.

Raja, M., Subha, J., Ali, F. B. and Ryu, S. H. (2008). Synthesis of copper nanoparticles by electroreduction process. Materials and Manufacturing Processes 23(8): 782–785.

Rostami, M., Badiei, A., Alijani, M., Das, A., and Ziarani, G. M. (2025). Nanoarchitectonic MOF-derived materials for enhanced photocatalytic activity in organic contaminant removal: A review. Alexandria Engineering Journal 126: 448-479.

Sangoremi A. A. (2025). Adsorption Kinetic Models and Their Applications: A Critical Review. International Journal of Research and Scientific Innovation 2(5): 245-258

Schneider, J., Matsuoka, M., Takeuchi, M., Zhang, J., Horiuchi, Y., Anpo, M., and Bahnemann, D. W. (2014). Understanding TiO_2 photocatalysis: mechanisms and materials. Chemical Reviews 114(19): 9919-9986.

Sharma, K., Shah, G., Singh, H., Bhatt, U., Singhal, K. and Soni, V. (2024). Advancements in natural remediation management techniques for oil spills: Challenges, innovations, and future directions. Environmental Pollution and Management 1: 128-146.

Sharma, P., Pandey, S., and Singh, R. (2021). Plant-mediated synthesis of calcium oxide nanoparticles: Characterization and applications. Environmental Nanotechnology Monitoring and Management 16: 1-23.

Singh, A., Mishra, S., and Patel, R. (2020). Green synthesis of CaO-CuO binary nanoparticles using Ocimum sanctum leaf extract for photocatalytic dye degradation. Ecotoxicology and Environmental Safety 202: 1108- 1133.

Singh, J., Kumar, V., Kim, K., and Rawat, M. (2019). Biogenic synthesis of copper oxide nanoparticles using plant extract and its prodigious potential for photocatalytic degradation of dyes. Environmental Research 177: 241- 269

Slosarczyk, A., Klapiszewska, I., Parus, A., Balicki, S., Kornaus, K., Gapiński, B., Wieczorowski, M., Wilk, K. A., Jesionowski, T., and Klapiszewski, Ł. (2023). Antimicrobial action and chemical and physical properties of CuO-doped engineered cementitious composites. Scientific Reports 13: 129 -152.

Soares, B. S., Borges, A. C., De Matos, A. T., Barbosa, R. B., and Silva, F. F. (2022). Exploring the Removal of Organic Matter in Constructed Wetlands Using First Order Kinetic Models. Water 14(3): 472-495.

Tiwari, P., Kaur, M., and Kaur, H. (2011). Phytochemical Screening and Extraction: A Review. Internationale Pharmaceutica Sciencia 1: 98-106.

Urooj Mariam, Sarmed Ali, Saba Jamil, Asima Saif, Hifza Arshad, Tahseen Kamal, Shaista Liaqat, Muhammad Jamshed Latif, Shanza Rauf Khan (2025). Synthesis, characterisation, and catalytic applications of CaO-Cu decorated PANI/SA nanocomposites for wastewater treatment, Materials Science in Semiconductor Processing 193: 19-48,

Usman Salifu Oma, Onoja Alexander David, Salihu Ali Audu, Momoh T.B., Buluku T. Gabriel and Okpanachi A.A (2022). Phytochemical Screening and Antibacterial Effect of Onion against Oral Pathogenic Bacteria. UMYU Journal of Pure and Industrial Chemical Research 2(2): 17-29

Zhang, Q., Zhang, K., Xu, D., Yang, G., Huang, H., Nie, F. and Yang, X. (2014). CuO nanostructures: Synthesis, characterization, growth mechanisms, fundamental properties, and applications. Progress in Materials Science 60: 208-337.

APPENDIX

Table 4.8: The Result of Physicochemical Characterization of the CaO-CuO binary nanoparticles treated petroleum wastewater (BTPEWW).

S/N	PARAMETERS	$BTPEWW_1$	$BTPEWW_2$	$BTPEWW_3$	SEM
1	Ph	6.20	6.40	6.20	6.27±0.36
2	Electrical conductivity (µs/cm)	267.00	266.00	268.00	267±0.47
3	Total Dissolved Solids (mg/L)	146.85	146.30	147.40	146.85±0.32
4	Temperature (^oC)	35.20	35.00	35.00	35.07±0.04
5	Total Suspended Solids (mg/L)	146.85	146.30	147.40	146.85±0.32
6	Total Solids (mg/L)	485.45	483.64	487.27	485.45±1.81
7	Chloride (mg/L)	246.14	241.82	238.96	242.31±2.09
8	Dissolved Oxygen (mg/L)	5.60	5.00	5.30	5.30±0.17
9	Biological Oxygen Demand(mg/L)	7.40	6.20	6.50	6.70±0.36
10	Chemical Oxygen Demand (mg/L)	106.74	112.32	110.19	109.75±1.63
11	Phosphate (mg/L)	9.74	10.30	10.30	10.11±0.19
12	Sulphate (mg/L)	24.55	27.16	23.34	25.02±1.13
13	Nitrate (mg/L)	64.22	57.98	60.31	60.84±1.82
14	Total Hydrocarbon (mg/L)	16.10	14.36	14.36	14.94±0.58
15	Turbidity (NTU)	56.78	50.53	52.79	53.37±1.83
16	Total Organic Carbon (%)	1.59	1.27	0.94	1.27±0.19
17	Cadmium (mg/L)	BDL	BDL	BDL	BDL
18	Lead (mg/L)	BDL	BDL	BDL	BDL
19	Nickel (mg/L)	0.10	0.14	0.10	0.11±0.01
20	Copper(mg/L)	0.30	0.29	0.32	0.30±0.01
21	Iron (mg/L)	3.20	3.00	2.78	2.99±0.12

Table 4.9: The Result of Physicochemical Characterization of the CuO nanoparticles treated petroleum wastewater (CuOPEWW).

S/N	PARAMETERS	$CuOTPEWW_1$	$CuOTPEWW_2$	$CuOTPEWW_3$	SEM
1	Ph	6.80	6.80	6.80	6.80±0.0
2	Electrical conductivity (µs/cm)	287	284	290	287±1.73
3	Total Dissolved Solids (mg/L)	157.85	156.20	159.50	157.85±0.95
4	Temperature (^oC)	35.00	35.00	35.00	35.00±0.00
5	Total Suspended Solids (mg/L)	ND	ND	ND	ND
6	Total Solids (mg/L)	157.85	156.20	159.50	157.85±0.95
7	Chloride (mg/L)	246.14	241.82	238.96	242.31±2.09
8	Dissolved Oxygen (mg/L)	6.10	6.00	6.00	6.03±0.03
9	Biological Oxygen Demand(mg/L)	8.20	7.90	8.10	8.07±0.09
10	Chemical Oxygen Demand (mg/L)	202.76	210.30	207.50	206.85±2.20
11	Phosphate (mg/L)	19.40	23.11	21.64	21.38±1.08
12	Sulphate (mg/L)	24.55	23.34	24.55	24.15±0.40
13	Nitrate (mg/L)	42.97	54.11	53.00	50.03±3.54
14	Total Hydrocarbon (mg/L)	23.74	28.20	26.10	26.01±1.29
15	Turbidity (NTU)	64.10	64.10	63.52	63.91±0.19
16	Total Organic Carbon (%)	3.20	4.00	3.20	3.47±0.27
17	Cadmium (mg/L)	BDL	BDL	BDL	BDL
18	Lead (mg/L)	BDL	BDL	BDL	BDL
19	Nickel (mg/L)	BDL	BDL	BDL	BDL
20	Copper(mg/L)	0.36	0.32	0.38	0.35±0.02
21	Iron (mg/L)	2.20	2.10	2.10	2.13±0.03

Table 4.9: The Result of Physicochemical Characterization of the CaO nanoparticles treated petroleum wastewater (CaOTPEWW).

S/N	PARAMETERS	**$CaOTPEWW_1$**	**$CaOTPEWW_2$**	**$CaOTPEWW_3$**	SEM
1	Ph	7.02	7.02	7.02	7.02±0.0
2	Electrical conductivity (µs/cm)	271	276	274	273.67±1.45
3	Total Dissolved Solids (mg/L)	149.05	151.8	150.7	150.52±0.80
4	Temperature (^oC)	32.00	32.00	32.00	32.00±0.00
5	Total Suspended Solids (mg/L)	ND	ND	ND	ND
6	Total Solids (mg/L)	149.05	151.8	150.7	150.52±0.80
7	Chloride (mg/L)	229.50	211.34	208.22	216.35±6.63
8	Dissolved Oxygen (mg/L)	5.90	6.00	6.00	6.03±0.03
9	Biological Oxygen Demand(mg/L)	8.20	7.90	8.10	8.07±0.09
10	Chemical Oxygen Demand (mg/L)	193.15	189.96	190.74	191.28±0.96
11	Phosphate (mg/L)	19.40	23.11	21.64	21.38±1.08
12	Sulphate (mg/L)	24.55	23.34	24.55	24.15±0.40
13	Nitrate (mg/L)	42.97	54.11	53.00	50.03±3.54
14	Total Hydrocarbon (mg/L)	30.36	31.00	30.78	30.71±0.19
15	Turbidity (NTU)	67.98	70.12	60.42	66.17±2.94
16	Total Organic Carbon (%)	4.20	3.80	4.00	4.00±0.12
17	Cadmium (mg/L)	BDL	BDL	BDL	BDL
18	Lead (mg/L)	BDL	BDL	BDL	BDL
19	Nickel (mg/L)	BDL	BDL	BDL	BDL
20	Copper(mg/L)	0.30	0.30	0.30	0.30±0.00
21	Iron (mg/L)	2.30	2.70	2.70	2.57±0.13